Low-Mass Planar Photonic Imaging Sensor
(A 2013-2014 NIAC Phase I Project)

Final Report

Submitted to NASA on June 3, 2014

by

S. J. Ben Yoo, Ryan P. Scott, and Alan Duncan

PRINCIPAL INVESTIGATOR:
Professor S. J. Ben Yoo
University of California
Dept. of Electrical and Computer Engineering
Kemper Hall, Rm 3179
Davis, California 95616
Tel: 530-752-7063
Fax: 530-752-8428
E-mail: yoo@ece.ucdavis.edu

Period Covered: October 1, 2013 – June 3, 2014

Contents

I.   Executive Summary

The Low-Mass Planar Photonic Imaging Sensor is based on the Segmented Planar Imaging Detector for EO Reconnaissance (SPIDER) concept developed in collaboration with Lockheed Martin Advanced Technology Center. SPIDER replaces the traditional optical telescope and digital focal plane detector array with a densely packed interferometer array based on emerging photonic integrated circuit (PIC) technologies that samples the object being imaged in the Fourier domain (i.e., spatial frequency domain), and then reconstructs an image. This approach replaces the large optics and structures required by a conventional telescope with PICs that are accommodated by standard lithographic fabrication techniques (e.g., CMOS fabrication). The standard EO payload integration and test process which involves precision alignment and test of optical components to form a diffraction limited telescope is, therefore, replaced by in-process integration and test as part of the PIC fabrication that substantially reduces associated schedule and cost.

This report covers the details of the Low-Mass Planar Photonic Imaging Sensor Concept and supports the discussions by presenting a prototype PIC that was developed under a DARPA funded effort. Then a SPIDER design tailored to a Europa mission is presented to show the improvements over a conventional Topographical Imager (TI), in which SPIDER collects $10\times$ the area on the surface of Europa with $17\times$ the resolution. The choices for PIC material platforms are investigated and specific designs for waveguides and integrated optical components are presented. SPIDER image modeling and reconstruction algorithms are explained and image simulations shown. Then initial experimental data from a prototype PIC are presented and discussed before a SPIDER technology roadmap is introduced.

II.   Technical Report Details

II.A.   Low-Mass Planar Photonic Imaging Sensor Concept

The Low-Mass Planar Photonic Imaging Sensor is an electro-optical (EO) imaging sensor concept that provides a low mass, low-volume alternative to the traditional bulky optical telescope and focal plane detector array. Figure 1 shows an approximate same-scale comparison of our Segmented Planar Imaging Detector for EO Reconnaissance (SPIDER) concept with a traditional telescope of comparable performance. This SPIDER concept was developed in collaboration with the Lockheed Martin Advanced Technology Center and consists of millions of direct detection white-light interferometers densely packed onto photonic integrated circuits (PICs) to measure the amplitude and phase of the visibility function at spatial frequencies that span the full synthetic aperture [1].
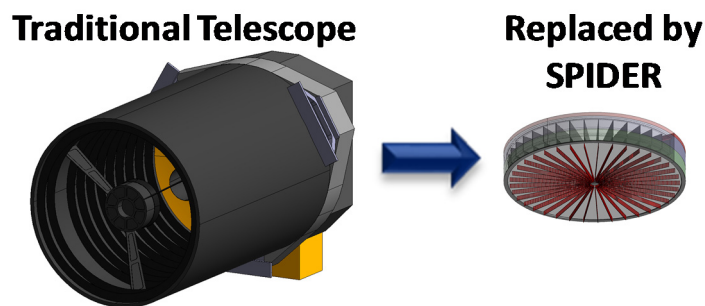
Figure 1. SPIDER is an innovative EO imaging sensor concept that replaces a traditional bulky optical telescope and focal plane with a low size, weight, and power densely packed photonic interferometer array that leverages rapidly developing nanophotonic technologies.

The conventional approach for imaging interferometers require complex mechanical delay lines to form the interference fringes resulting in designs that are not traceable to more than a few simultaneous spatial frequency measurements [2]. SPIDER achieves this traceability by employing micron scale optical waveguides and nano-photonic structures fabricated on a PIC with micron scale packing density to form the necessary interferometers. It is straightforward to include spectral filters, optical phase modulators, photodetectors and possibly even electronics on the same chip. Our approach replaces the large optics and structures required by a conventional telescope with PICs based on emerging photonic technologies which are produced by standard lithographic fabrication techniques (e.g., CMOS fabrication). This means that the standard EO payload integration and test process that involves precision alignment and test of optical components to form a diffraction-limited telescope is, in essence, replaced by in-process integration and test as part of the PIC fabrication. Thus, similar to the reductions achieved in the transition from CRT televisions to lightweight, thin LCD screens, we expect a 10−100× reduction in the EO imager's size and mass and a substantial reduction in the associated schedule and cost of space telescope deployment, affecting a range of future NASA missions.

The SPIDER concept samples the object being imaged in the Fourier domain (i.e., spatial frequency domain), and then digitally reconstructs an image. Figure 2 shows an example SPIDER design that has a top layer consisting of a lenslet array covered by multi-aperture baffle plate to control stray light. Below the lenslets are PIC "cards" in a radial pattern which contain the nano-photonic delay lines, phase modulators, and beam combiners, followed by a second layer consisting of detectors and readout electronics, and a third layer that processes the raw data

and outputs image data. The lenslets and PIC cards are arranged to uniformly sample the object's spatial frequencies.
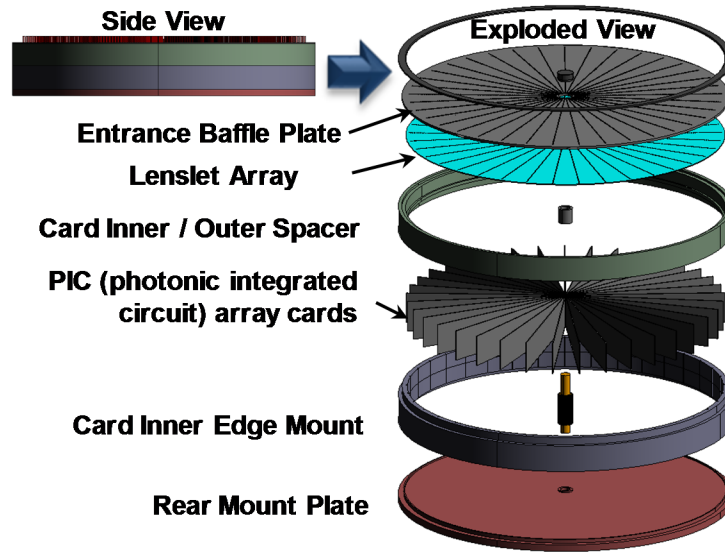
Figure 2. Conceptual image of the SPIDER EO imaging sensor showing major elements.

Figure 3(a) depicts a single lenslet array above a PIC card and Figure 3(b) shows a close-up of the waveguide input array that is at the focal plane of a single lenslet. In our SPIDER concept, each waveguide collects light from a different field point in the scene (shown as different colored focusing beams) and common points in the scene from pairs of lenslets are combined to create fringes measured by the photodetection electronics. The phase and amplitude is recorded for each field point and each lenslet pair which form a baseline. The various baseline data are placed in the *uv*-plane (i.e., the virtual Fourier plane) array at the proper location in order to reconstruct the scene that is being imaged.
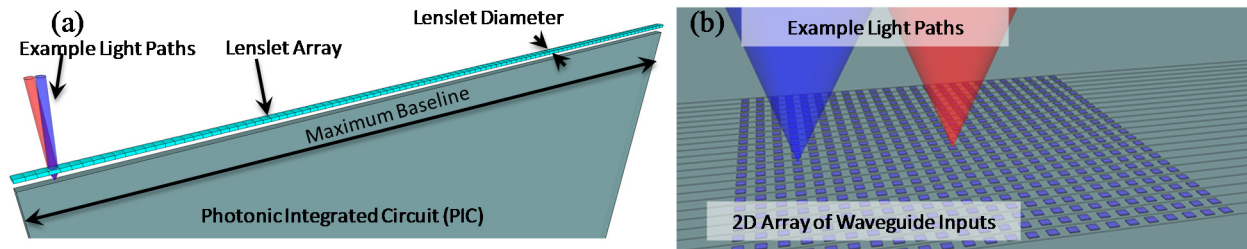
Figure 3. (a) Detail of a lenslet array and PIC card. (b) Close-up view of 2-D waveguide input array at the lenslet image plane.

To better understand the operation of the PIC, Figure 4 shows the schematic view of a prototype PIC with a limited number of baselines. It has two interferometric baselines, one with a 20 mm separation and the other with 5 mm separation. Behind each lenslet is an array of five waveguide inputs that sample different field points on the object. The light from each pair of waveguides from lenslets that form an interferometer pair are demultiplexed into wavelength bins (e.g., three 20-nm wide spectral bins near 1550 nm) and combined with variable phase shifts to enable a measurement of the complex visibility. Each wavelength bin provides a unique spatial frequency to further fill the *uv*-plane. The complex visibilities from all the measurements are then processed to form an image.
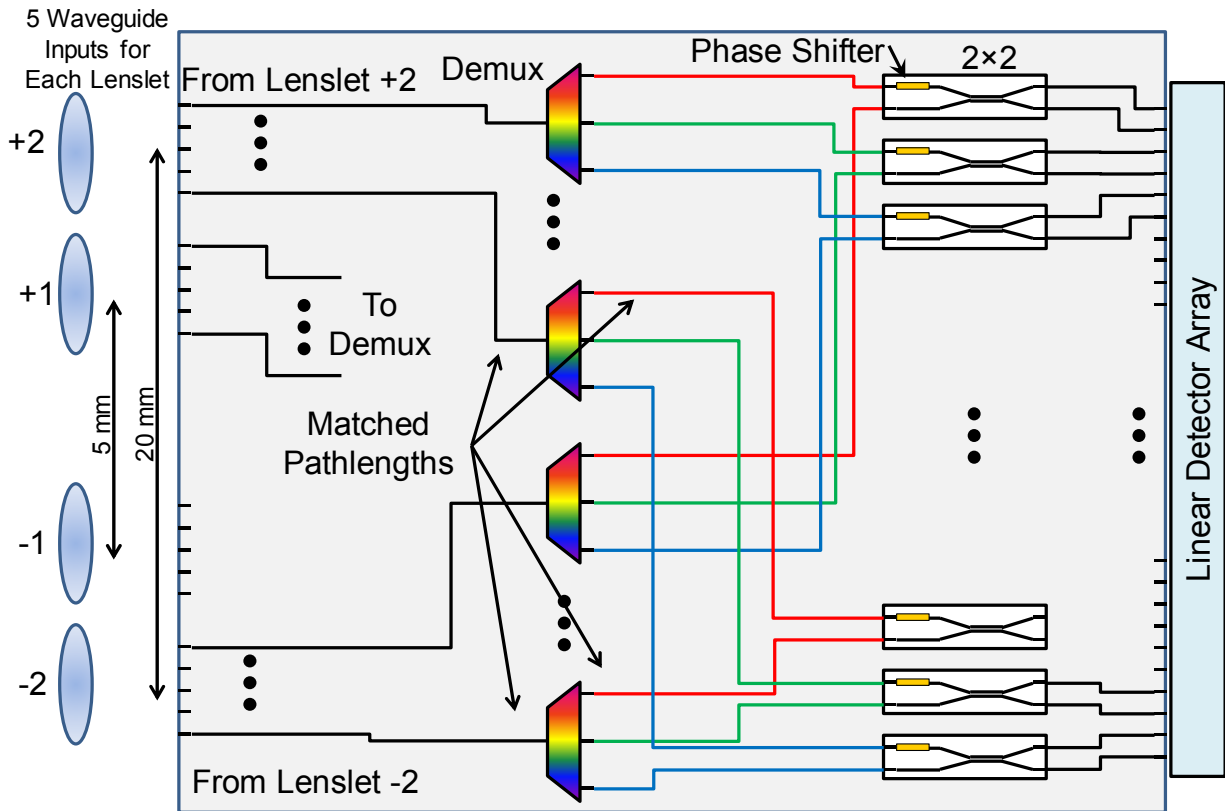
Figure 4. Schematic view of a prototype PIC with two baselines, three spectral bands, and five input waveguides behind each lenslet (i.e., samples five different object points).

Figure 5 presents the silica-on-silicon PIC layout (1.5% index contrast) [3, 4] that corresponds to the schematic above (design and fabrication funded by DARPA). The green traces show the waveguide layer with inputs on the left and outputs on the right. After the input waveguides, cascaded asymmetrical Mach-Zehnder interferometers (MZIs) form the spectral demultiplexers. Following the spectral demultiplexers are the phase shifters based on thermo-optic refractive index changes using resistive heaters above the waveguides and they include heat-isolating trenches on either side of the waveguide. The 2×2 interferometers combine the light from corresponding waveguide inputs and spectral bins and their two output waveguides are tapered wider to increase the optical mode size (i.e., lower the numerical aperture) before detection by a linear detector array butt coupled to the edge of the PIC. There are also smaller thermo-optic tuners on the asymmetric MZIs to adjust the center wavelength of the spectral passbands.
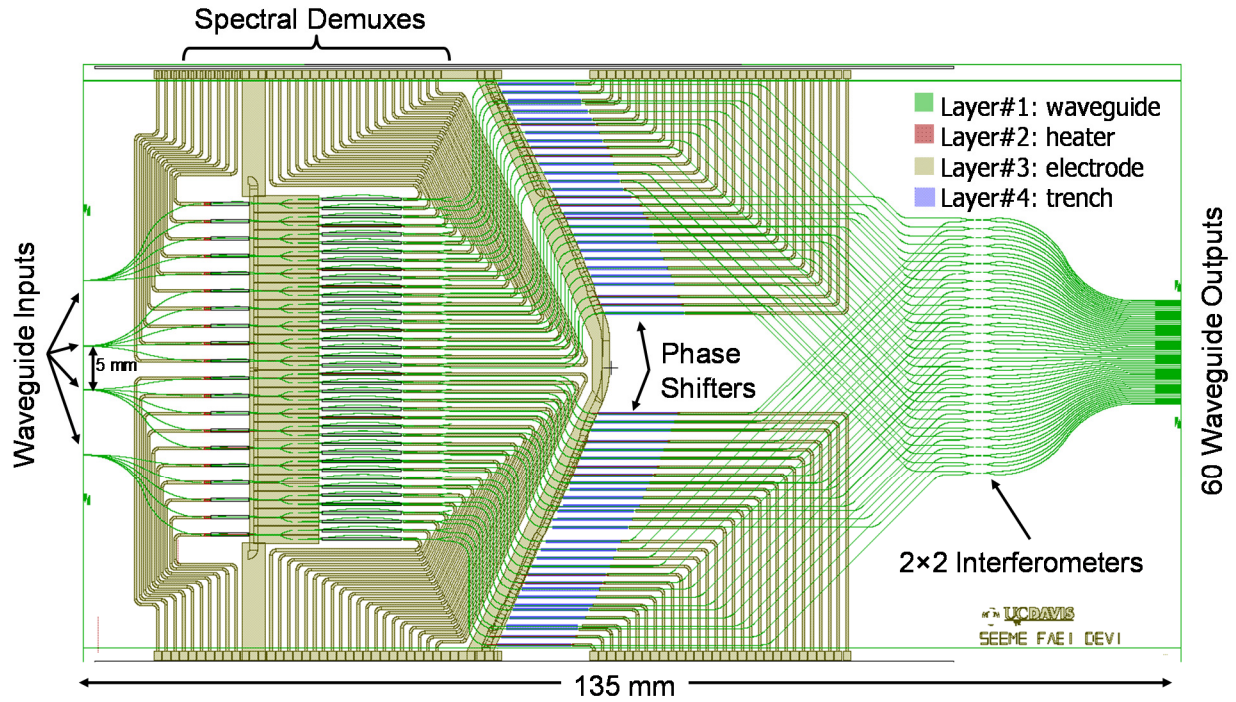
Figure 5. Layout of the prototype PIC shown schematically in Figure 4.

Figure 6 shows a photo of the prototype PIC with the lenslets and linear detector array in place.
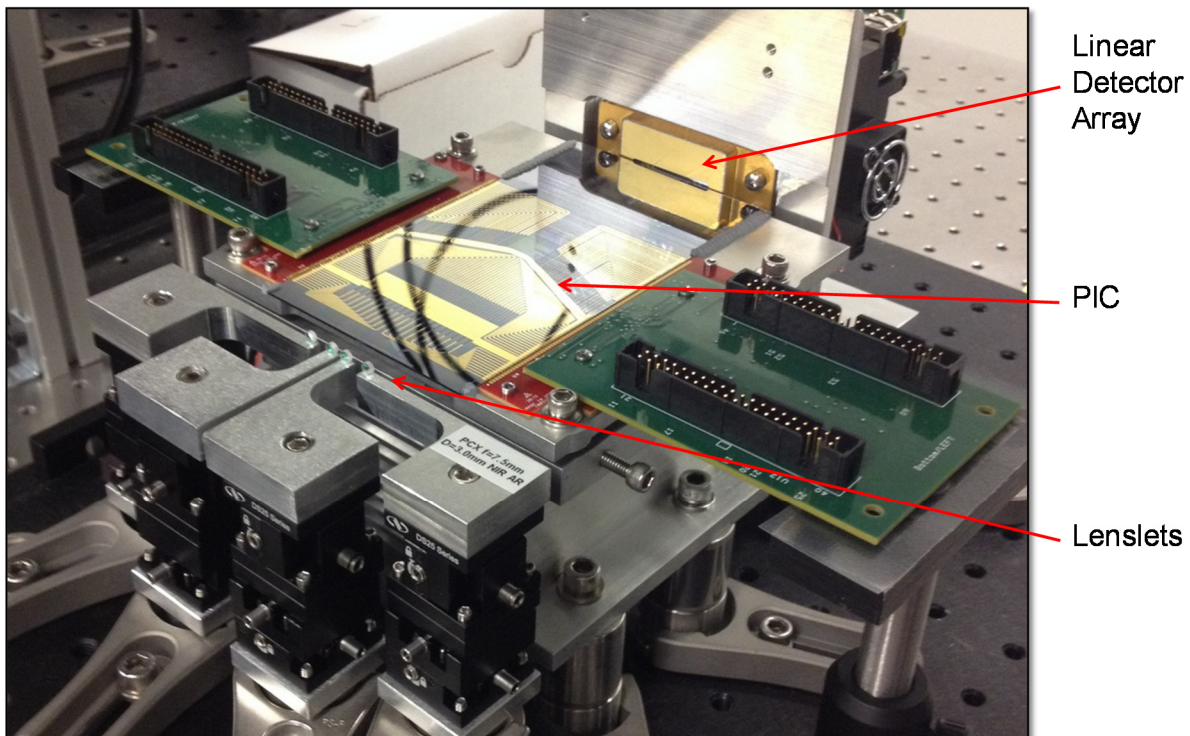
Figure 6. Photo of prototype PIC with lenslets, and linear detector array.

Later sections present additional details of the prototype PIC and some initial experimental work based on the device.

II.B. SPIDER design tailored to a Europa mission

Exciting new NASA missions will be enabled by the SPIDER concept since it provides a large-aperture, wide-field EO imager at a fraction of the cost, mass and volume of conventional space telescopes, by integrating advanced optical interferometry and photonics technologies. The SPIDER EO imager concept provides high-resolution images and long dwell times at high altitudes, thereby enabling real-time, wide-area remote sensing of dynamic changes in planet surface processes. These remote sensing capabilities significantly enhance astrobiologic, geologic, atmospheric, and similar scientific objectives for planetary exploration missions. Of particular interest to NASA, a Jupiter icy moons orbiter mission [5, 6] with the SPIDER concept imager would enable imaging data with far greater breadth and depth than previously possible for a particular cost. Figure 7 provides an overview of a Jupiter icy moons mission study performed by our team to assess the science impact of a higher resolution EO imaging sensor. This particular study assumed a 1.5-m-aperture imaging sensor and explored the science gain as a function of resolution.
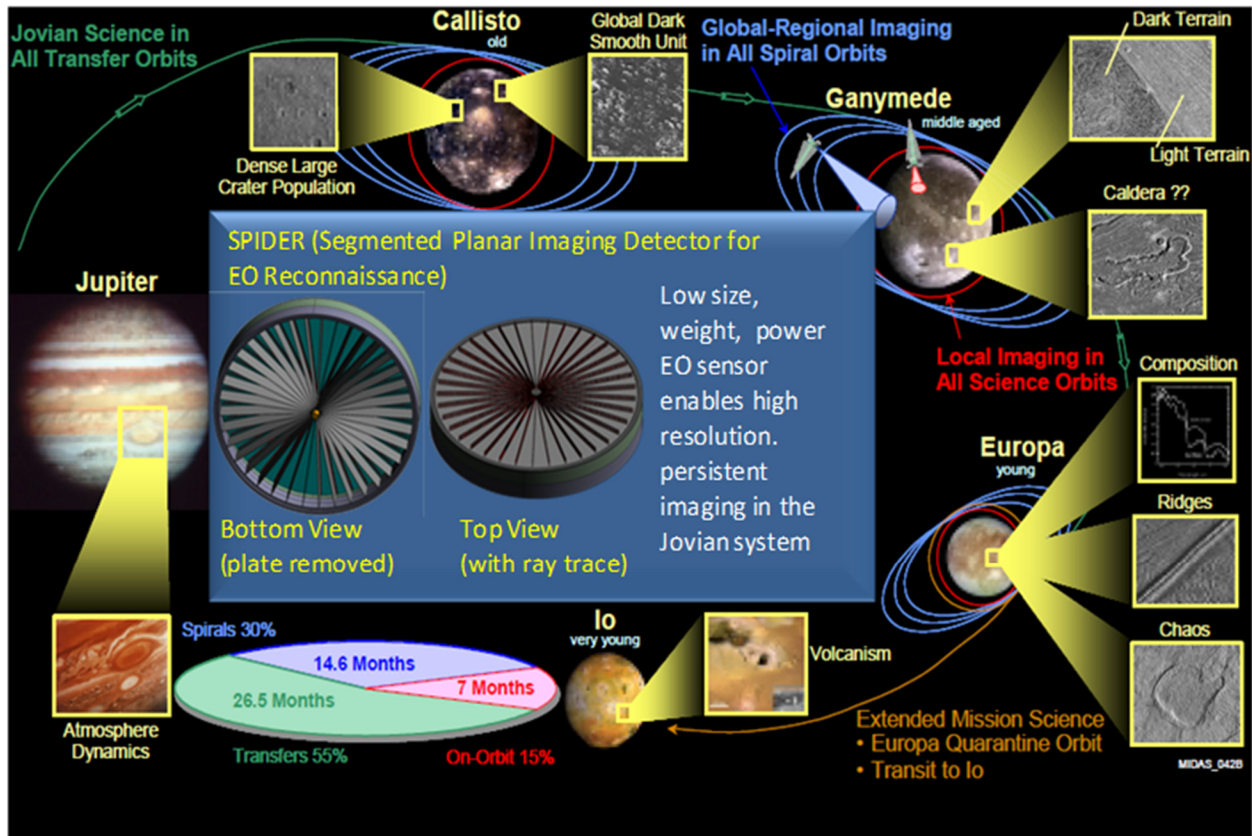
Figure 7. Overview of a Europa orbiter mission with a SPIDER EO imaging sensor.

The sensor design features high-resolution imaging for long dwell times at high altitudes (e.g., <1-m ground sample distance (GSD) from the 5,000 km extent of spiral orbits) enabling regional remote sensing of dynamic planet processes. At lower altitudes, this becomes ultra-high

resolution imaging (e.g., <2-cm GSD from the 100 km science orbits) enabling remote sensing searches for life sign processes. Figure 7 shows an example Jovian system mission scenario with key capabilities highlighted that are enabled by the unique features of our SPIDER imaging sensor.

Figure 8 shows the results, with an emphasis on Europa. The curve shows the resolution versus range and the available contact with objects of interest in the Jovian system. The capability of 2 cm GSD resolution from a 100 km science orbit at each of Jupiter's icy moons is highly leveraged by proceeding and following each of those science orbits with months of observations. These observations are taken at <1 m GSD resolution that is achieved during the inward and outward spiral orbits extending to 5,000 km altitude. In addition, remote sensing at higher altitudes during the entire four years spent in the Jovian system, with resolutions of 2 cm to 200 m GSD for each icy moon, 50 m to 300 m for Io and 150 m to 400 m for Jupiter, as shown in Figure 8.
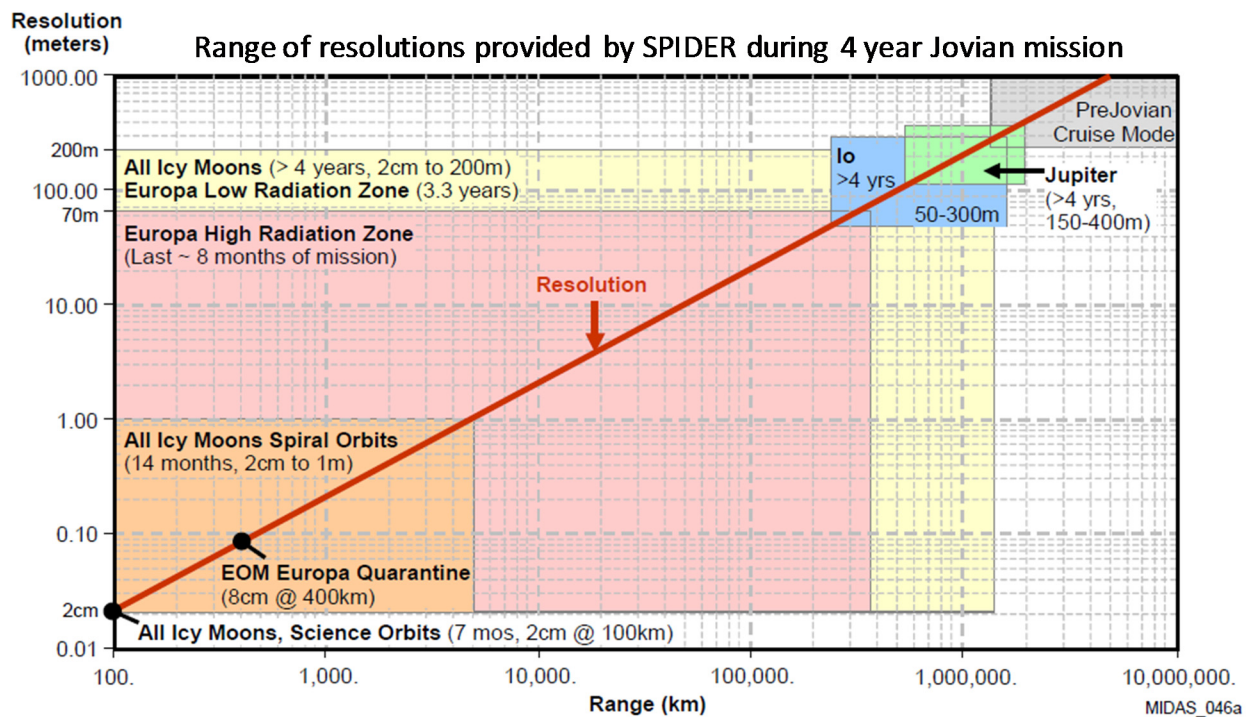
Figure 8. Performance of a SPIDER 1.5-m aperture EO imaging sensor for a Jupiter icy moons mission.

The large aperture diameter for this mission study is beyond what is currently envisioned for the SPIDER concept due to limitations on the ability to fabricate large area photonic integrated circuits and the propagation losses over long distances in the chip. To evaluate the mission utility of a SPIDER EO imaging sensor, we selected a Europa orbiter reference mission [5]. This mission is particularly suited for this study as the size, weight, and power of the imaging sensor is a key driver for performance (resolution and area collection) due to the high cost of delivering a payload into a Europa orbit. Therefore, we focused on a closer range mission that featured a smaller aperture EO imager, Europa Clipper. Specifically, SPIDER was evaluated as a replacement for the Topographical Imager (TI), shown in Figure 9.

- **Proposed Traditional Imager**
    - **250 μrad IFOV → 25 m Ground-Sampled-Distance (GSD) at 100 km**
    - **4096 detectors, 5.5-ms integration time**
    - **Push-broom mode collection**
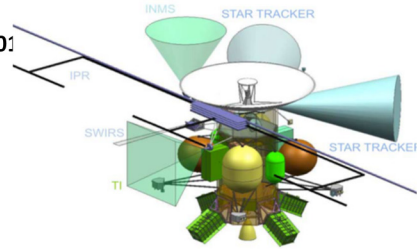
Figure C.2.2-1. Notional model payload accommodation and fields of view.

Diagram of Europa's ice shell
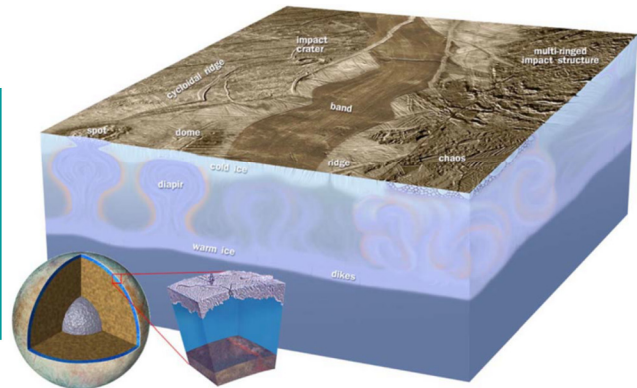
Similar Imagers

MRO Mars Color Imager (MARCI)
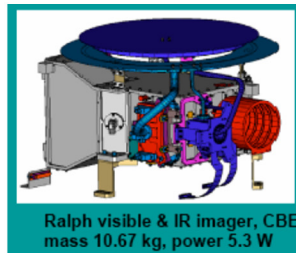
New Horizons Multi-spectral Visible Imaging

Ralph visible & IR imager, CBE mass 10.67 kg, power 5.3 W

Figure 9. Reference mission for SPIDER mission utility study.

The currently proposed TI is a small aperture EO imager for imaging large areas of Europa's surface. Its aperture size and resolution are limited by size, weight, and power (SWaP) constraints that include the requirement to provide radiation shielding. We propose a SPIDER version of the TI that we constrain to fit into the radiation shielded volume for the current design. The intent of the study is to see what performance advantages can be achieved with SPIDER with the current TI SWaP constraints. A 4-cm aperture SPIDER is achievable within those constraints, as shown in Figure 4. The 4-cm aperture SPIDER includes a detector array that is equivalent to a conventional 10-megapixel image with a 150-ms integration time.

- **SPIDER Topographical Imager**
  - **4 cm** diameter aperture (same enclosure)
  - **15 μrad IFOV → 1.5 m** Ground-Sampled-Distance (GSD) at 100 km
  - **10 Mpixel area, 150-ms integration time**

For the same mass, SPIDER could collect 10× the area on ground with 17× the resolution

NASA Photojournal PIA03002

Europa's Ridges

NASA Photojournal PIA01182

NASA Photojournal PIA00589
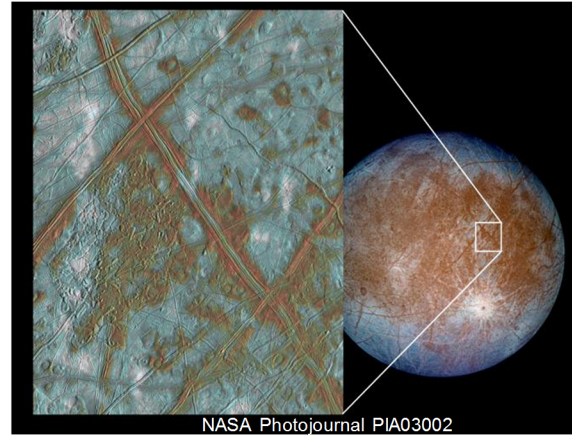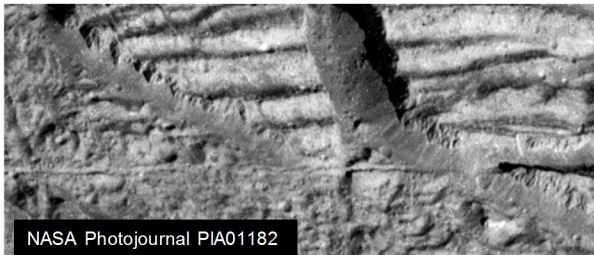
Figure 10. SPIDER design optimized to fit current TI SWaP constraints.

A comparison was made to the current TI predicted performance. SPIDER collects 10× the area on the surface of Europa with 17× the resolution.

Figure 11 provides a more detailed description of the predicted performance of the current TI design. The limited resolution of the TI provides only 16 minutes of image collection time per flyby due to the highly elliptical orbit. There is, therefore, opportunity for significant increases in data collection rates if the resolution of the sensor can be improved. This is also true of the SWIR sensor that was not investigated for this study. Our SPIDER concept permits compact, low SWaP imaging sensors at longer wavelengths including SWIR and MWIR. We are currently working with DARPA to design and build an IR proof of concept demo for SPIDER.

Table C.2.5-1. Instrument on times per flyby.

Altitude Range (km)	Time at Altitude (minutes)	Instrument On Time (minutes)			
		IPR	TI	SWIRS	INMS
66,000 to 2,000	265			265	
2,000 to 1,000	5			5	
1,000 to 400	4	4	4	4	4
400 to CA	4	4	4	4	4
CA to 400	4	4	4	4	4
400 to 1,000	4	4	4	4	4
1,000 to 2,000	5			5	
2,000 to 6,000	265			265	
Total Minutes	**554**	**15**	**15**	**554**	**15**

Current projected capability provides only 16 minutes of TI imagery per flyby SWIRS has similar limitation for high resolution mode

Figure C.2.5-1. Europa encounter concept—Multiple-Flyby Mission.

Figure 11. Details of current TI performance predictions.

Our estimated performance for SPIDER is based on a mission concept of operations that takes advantage of the higher resolution of the sensor to enable data collection over more of the orbit and collection of higher resolution images near the region of closest approach. Figure 12 shows the orbit geometry.
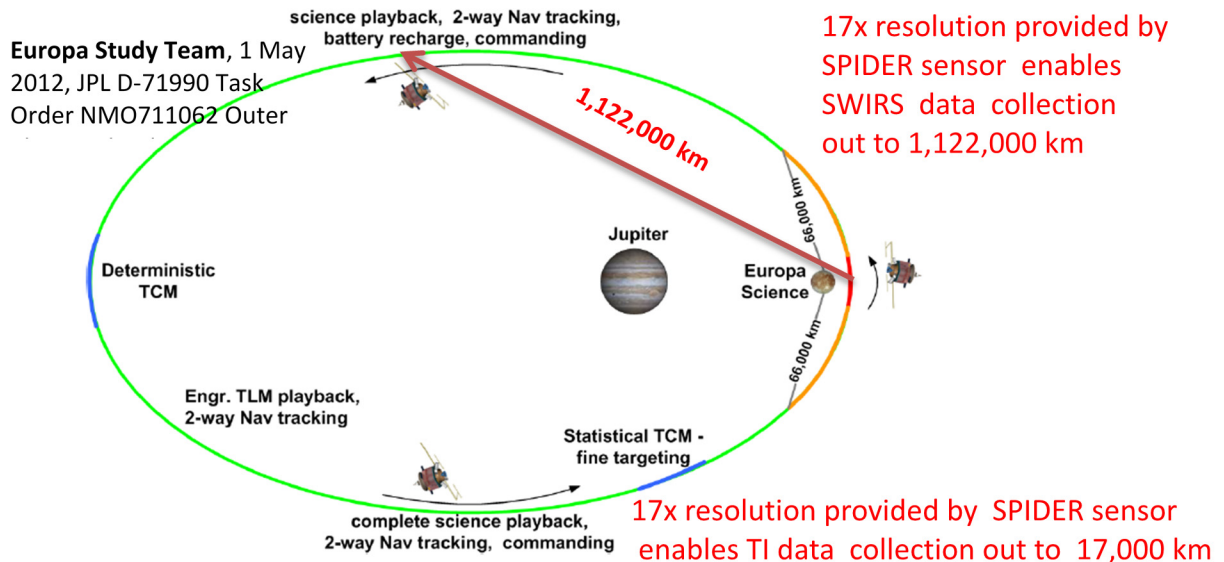
Figure 12. Europa orbit with SPIDER imaging sensor performance enhancement.

SPIDER's improved resolution provides imagery with resolution comparable to the current TI instrument at a range of 1,122,000 km and resolution 17× higher than TI at a range of 17,000 km. By accommodating an image frame size that is substantially larger than the TI push-broom image swath, SPIDER also improves the area coverage by increasing both the length (17×) and width (5×) of the image swaths for each flyby pass. Figure 13 illustrates the current TI imaging performance in terms of coverage and resolution.
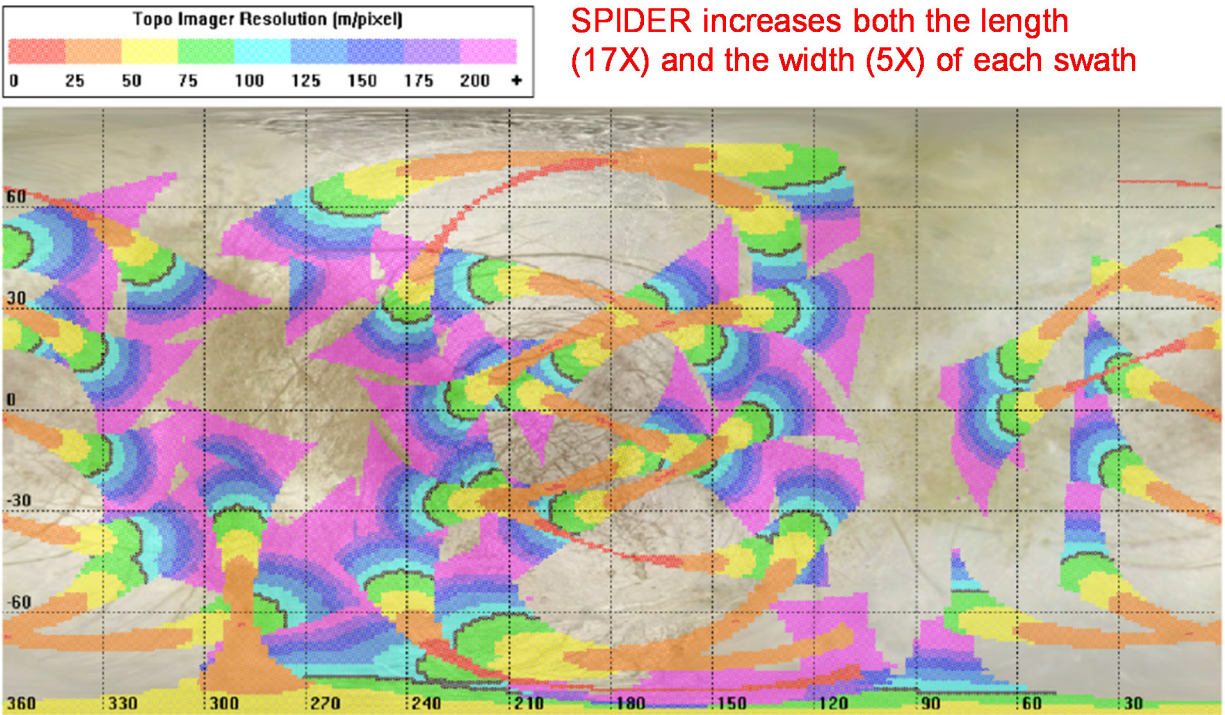
Figure C.2.5-6. TI instrument coverage.

Europa Study Team, 1 May 2012, JPL D-71990 Task Order NMO711062 Outer Planets Flagship Mission

Figure 13. Predicted imaging performance of the current TI instrument.

For both the TI and SWIR Europa Clipper instruments, SPIDER increases the imaging time per flyby orbit from 16 minutes to 272 minutes that enables substantially higher area coverage of Europa's surface.

For these analyses, we made conservative assumptions for the SPIDER integration times. Although performance will improve as the technology advances, current versions of the SPIDER photonic integrated circuits have significant throughput losses. Therefore, the integration time for SPIDER was increased from 5.5 ms to 150 ms to account for these losses. Given this integration time, SPIDER's performance compared to the TI increases the area collection rate from 745 GSD^2 to 17,000 GSD^2 and increases the effective scan rate, at an altitude of 1,000 km, from 170 km^2/s to 15,000 km^2/s.

II.C. Photonic integrated circuit (PIC) material platforms

II.C.1. PIC material choices

Although the benefits of integrated photonic devices for optical communications applications are well known and highly exploited, their potential in imaging applications has received limited attention. However, due to the sophisticated and numerous routing requirements of the SPIDER concept, a practical implementation requires the performances available in an integrated platform. Many PIC applications, including telecommunications, require the compactness, stability, efficient collection, routing, filtering, and interfering of single moded light waves, but the sheer scale required for the envisioned SPIDER concept poses new challenges. Further, telecommunications applications have driven PIC development in the 1.3 µm and 1.55 µm

spectral regions, but other spectral regions are far less mature but of potentially greater interest for imaging applications.

Whether a particular material is a candidate for inclusion in an integration platform is determined by its transparency window and on the losses (intrinsic and extrinsic) within this window. Figure 14 presents the transmission range for over a dozen prospective materials that provide a relatively large window in the visible and/or infrared part of the spectrum. A material's intrinsic losses, which represent a minimum expected loss, depend on its electronic transitions, phonon interactions and free-carrier effects. Extrinsic losses in the form of impurities and defects, whether admitted during material growth or during device fabrication, will further reduce the transmission and these losses generally dominate. An excellent example of this is fused silica and its use in the telecommunications industry. Many years of manufacturing technology refinement have created silica fibers with such a high level of purity and quality that the material losses closely approach intrinsic levels. Although fused silica may be the most widely used PIC material, the ultrawide windows (i.e., visible through mid-wave infrared) of fluoride glasses (BaF$_2$, MgF$_2$, CaF$_2$, and ZBLAN), sapphire and zinc selenide are particularly attractive. Unfortunately, fabrication techniques for large scale integrated photonic circuits in these materials still need to be developed.
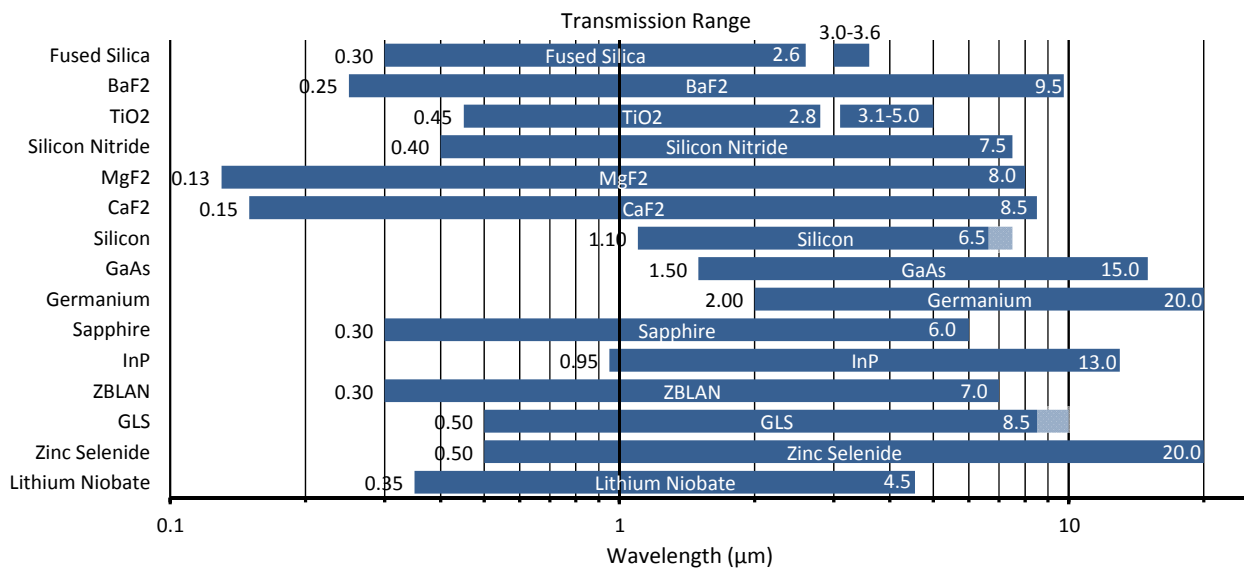
Figure 14. Transmission range of selected materials.

For many space-based imaging applications, high optical throughput (i.e., low system losses) are particularly important. Silica-on-silicon PICs (i.e., silica planar lightwave circuits PLCs) have been the most successful in meeting the challenge since they have losses <0.02 dB/cm at $\lambda = 1550$ nm for bend radii >2 mm (1.5% core-cladding index contrast) [4]. This relatively low-index-contrast core is typically embedded between $10-20$ μm of fused silica (SiO$_2$) as an upper and lower cladding. To ensure low polarization sensitivity and efficient single-mode fiber coupling for telecommunication applications, the core is symmetric and $4-5$ μm in width/height. The major drawback with silica-on-silicon PICs is its low index contrast and correspondingly large minimum bending radius (i.e., too small of a bending radius results in radiation losses from the waveguide). This relatively large minimum bend radius requirement means that PIC dimensions will be orders of magnitude larger than waveguide or optical mode cross-section.

However, it is well suited for use in the visible (0.4-0.75 μm), near infrared (NIR, 0.75-1.4 μm) and most of the short-wave infrared (SWIR, 1.4-3.0 μm) band and fully commercialized. Thus, we use it for the prototype PIC shown in Figure 5.

A material with a large transmission window is stoichiometric silicon nitride (Si_3N_4) which has an index of refraction of 1.98 at $\lambda = 1550$ nm. When combined with fused silica as a cladding material ($n = 1.44$), the high index contrast (~25%) provides small minimum bending radii. It is well known that high-index-contrast waveguides typically suffer significant extrinsic losses due to sidewall scattering [7]. However, a high-aspect-ratio core geometry, where the waveguide width far exceeds its thickness, is effective at minimizing these losses [8]. The tradeoff with such thin waveguides (~100 nm or less) is a much lower confinement factor and therefore a larger minimum bend radius. Reports in the literature show that <0.01 dB/cm is possible when minimum bend radii are relatively large (~10 mm), but still a very reasonable 0.1 dB/cm when the bend radius is ≤0.5 mm [8].

Both silica-on-silicon and silicon nitride material platforms use CMOS-compatible fabrication equipment which provides a direct path to large-scale photonic integration in future versions of SPIDER. Larger 450-mm silicon wafer production, currently under development, enables future versions of SPIDER that implement these large two-dimensional interferometer arrays on a single monolithic silicon wafer.

II.C.2. Si₃N₄ waveguide designs

To verify the feasibility of a Si_3N_4:SiO_2 waveguide platform, we perform some simulations and analysis of optimal waveguide and component parameters with a design wavelength of 1550 nm in the SWIR. Figure 15 shows the waveguide geometry used for the rest of the analysis. The core is kept thin (200 nm) to reduce losses, but it is still thick enough to keep the minimum bend radius <0.5 mm.
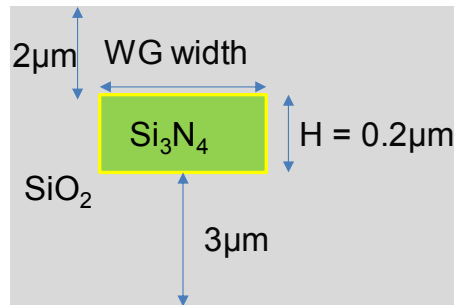
Figure 15. Geometry of the Si_3N_4 waveguide embedded in fused silica.

Figure 16(a) shows the confinement factor and (b) effective index as a function of the WG width. The discontinuity at ~2.2 μm for Mode 2 indicates it becomes a supported mode for widths >2.2 μm (200 nm WG height). Therefore we use 2-μm wide waveguides to ensure single-mode operation.
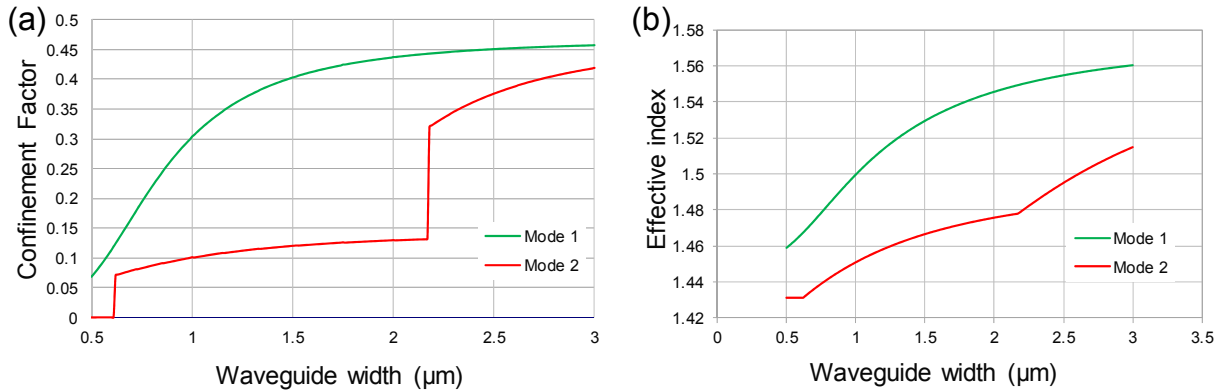
Figure 16. Simulation of a Si₃N₄ waveguide to determine single mode operation region (200 nm height, λ = 1550 nm.)

Figure 17 shows simulated optical mode profile (TE polarization) for the 2 µm-wide × 0.2 µm-tall SiN waveguide. The intensity mode profile is on the left (amplitude contours on right) with a $1/e^2$ diameter of 2.64 µm (horizontal) and 1.69 µm (vertical).
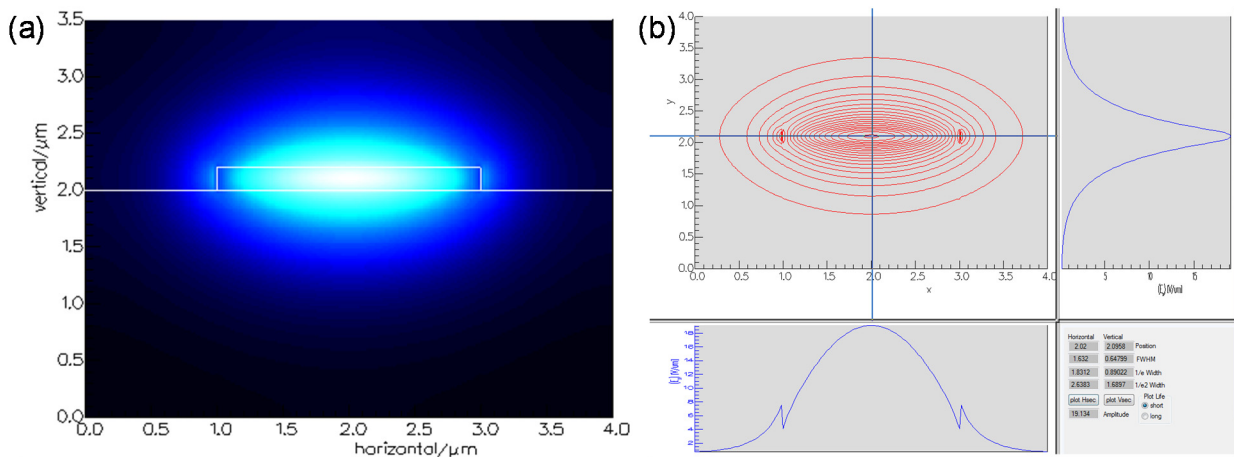
Figure 17. Detailed mode profile for TE polarized light in a SiN waveguide, 2-µm wide × 0.2-µm tall.

Figure 18 shows a bend radius analysis for the 2 µm wide × 0.2 µm tall SiN waveguide. Figure 18(a) shows the mode profile in the middle of a 50-µm bend and Figure 18(b) shows the mode profile in the middle of a 150-µm bend. Although the loss is quite small for a 50-µm radius bend, the mode profile is symmetrical and much better matched to straight waveguides for a 150-µm radius bend. Therefore, a minimum bending radius of ~150 µm is chosen. This minimum bending radius is ~10 times smaller than typical silica devices.
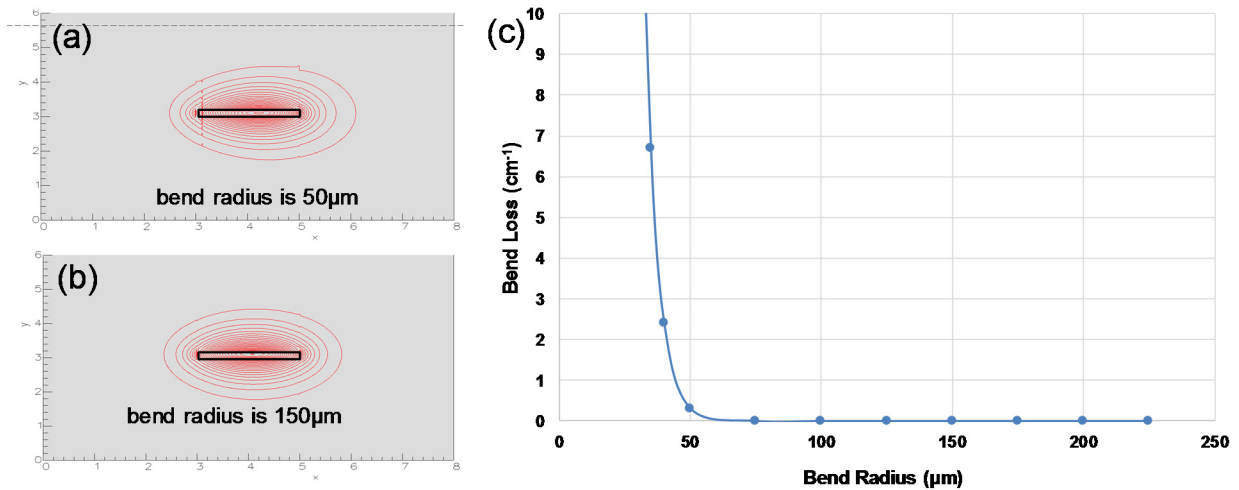
Figure 18. Bend radius analysis for a 2-µm wide × 0.2-µm tall SiN waveguide. (a) Mode shape in the middle of a 50-µm radius bend. (b) Mode shape in the middle of a 150-µm radius bend. (c) Bend loss as a function of bend radius.

Figure 19 shows the effective index (TE polarization) of the silicon nitride waveguide (2 µm wide × 0.2 µm tall) across the design wavelength range. Due to the low confinement factor, it has an effective index much closer to the cladding than the core.
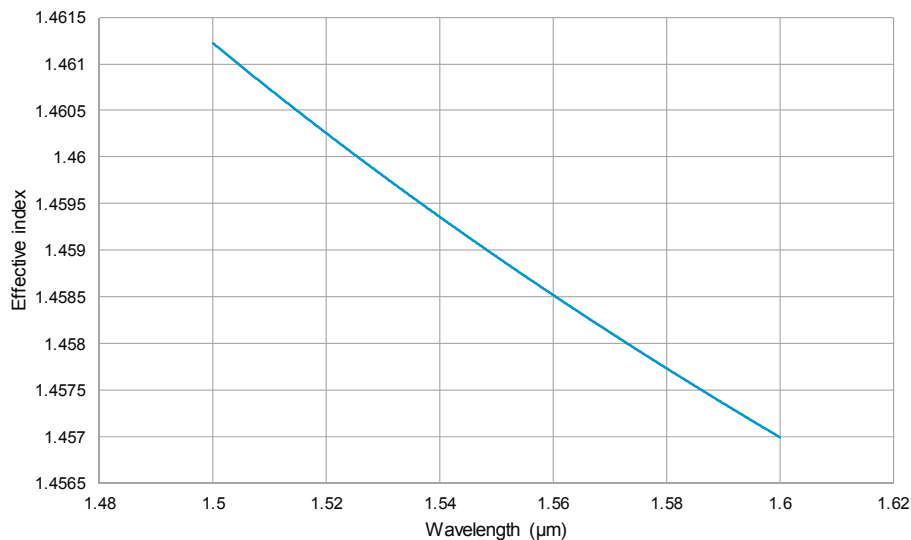
Figure 19. Effective index of the silicon nitride waveguide at 1550 nm ±50 nm (2-µm wide × 0.2-µm tall).

II.C.3. Si₃N₄ component designs

As Figure 4 shows, a SPIDER imager PIC requires several components including thermo-optic phase shifters, 1×2 and 2×2 splitters. Figure 20 shows the thermal-optic phase shifter tuning simulation parameters for a silicon nitride waveguide with 2-µm width when the top cladding thickness is 1 µm or 2 µm. The phase due to thermal heating goes as $\Delta\varphi=(2\pi/\lambda)\times L_h\times(\Delta n/\Delta T)\times\Delta T$ where λ is 1550 nm.

Material	Thermal Conductivity [W/(m*K)]	Density [kg/m³]	Heat Capacity [J/(kg*K)]	dn/dT
Si_3N_4	33	3200	710.6	0.4×10^{-4}
Silica	1.38	2203	703	1.477×10^{-5}
Air	0.026	1.166	1005	-
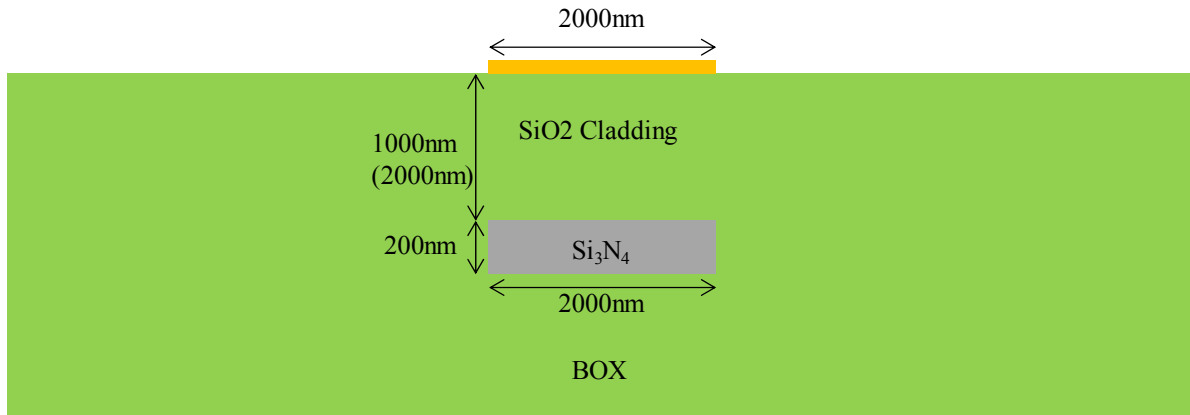
Figure 20. Thermo-optic phase shifter tuning simulation parameters for a silicon nitride waveguide with 2-μm width. The top cladding is assumed to be 1 μm or 2 μm.

Figure 21 shows the simulation results for a heater length of 1000 μm and a width of 2 μm for two different top cladding layer thicknesses, 1 μm (red) and 2 μm (black). The heater is made from platinum and its height is 200 nm. The left plot shows the optical phase change is linear with heater power (proportional to the current squared). The right plots shows the optical phase change as a function of heater current. The power for π rad phase shift is ~80mW (1 μm) and ~100 mW (2 μm).
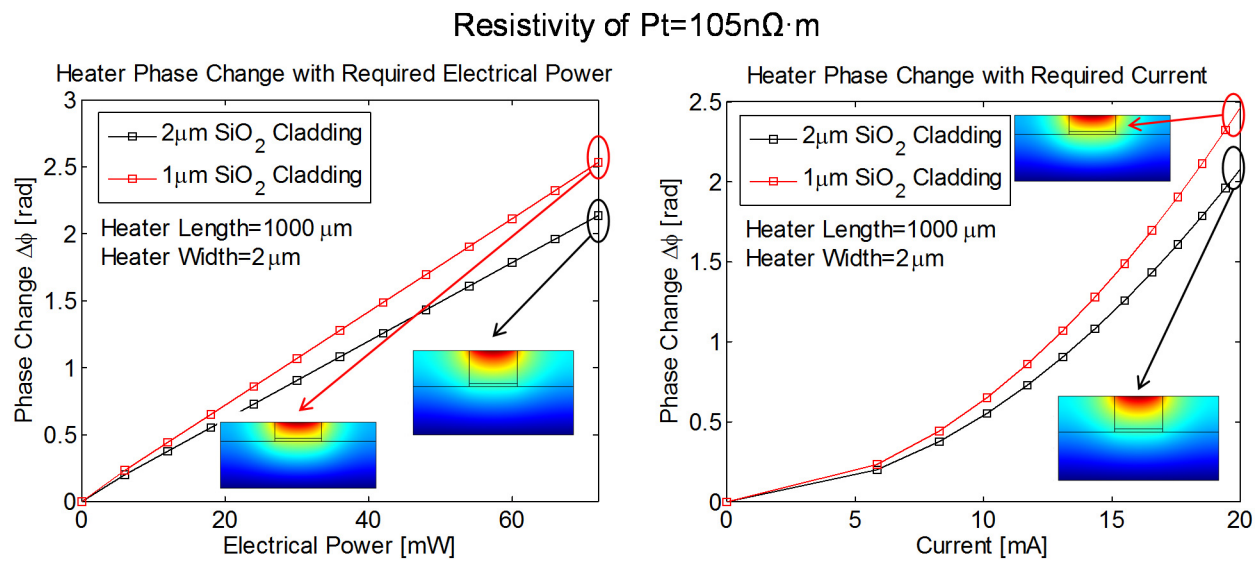
Figure 21. Si_3N_4 waveguide thermal simulations for Ti/Pt (20nm/200nm) heater.

Figure 22 shows the parts of a Si$_3$N$_4$ 1×2 multi-mode interference (MMI) coupler that is used to equally split the light into two waveguides.
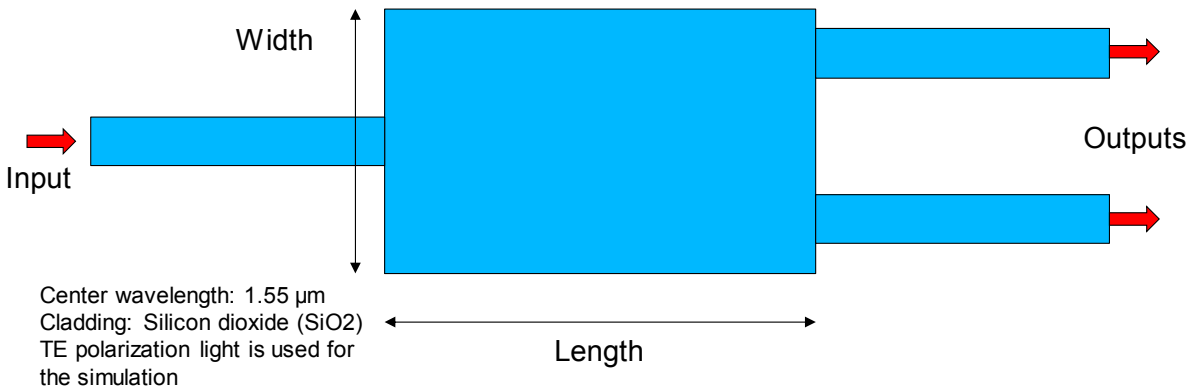
Figure 22. Schematic of a Si$_3$N$_4$ 1×2 multi-mode interference (MMI) coupler.

Figure 23 shows a simulation of the optimized Si$_3$N$_4$ 1×2 MMI design with nearly perfect 50% (e.g., 49.8%) power coupling to the two output ports.
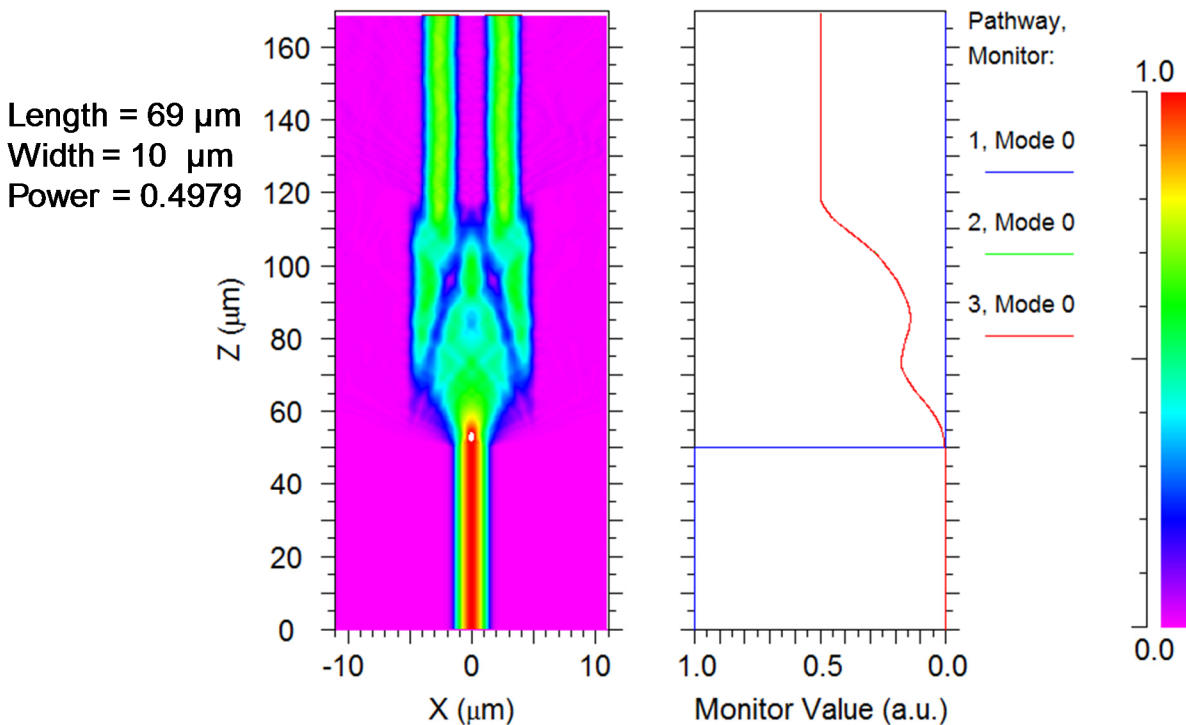
Figure 23. Si$_3$N$_4$ 1×2 MMI simulation.

Figure 24 shows the parts of a Si$_3$N$_4$ 2×2 multi-mode interference (MMI) coupler.

Input

Width

Length

Center wavelength: 1.55 µm
Cladding: Silicon dioxide (SiO2)
TE polarization light is used for
the simulation
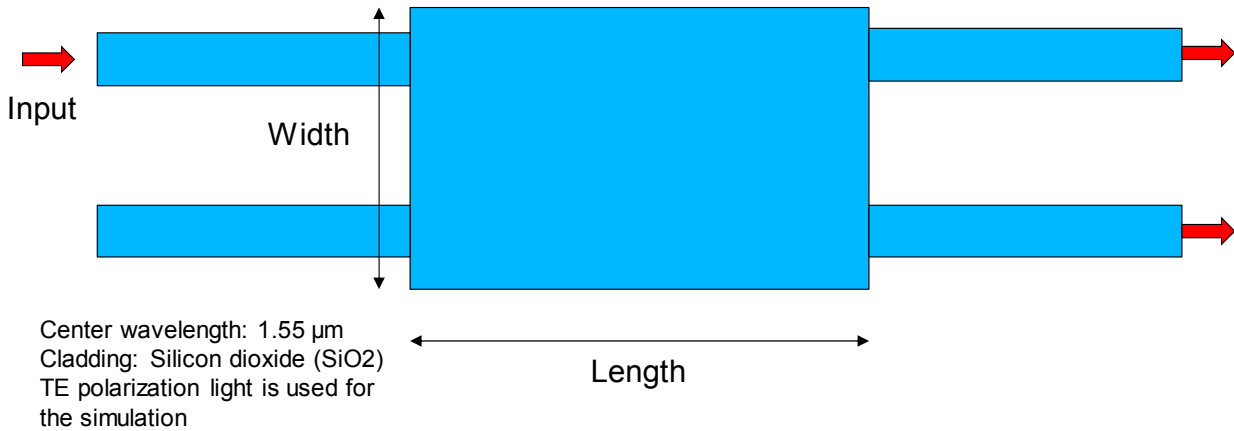
Figure 24. Schematic of a Si₃N₄ 2×2 multi-mode interference (MMI) coupler.

Figure 25 shows a simulation of the optimized Si₃N₄ 2×2 MMI design with nearly perfect 50% (e.g., 49.82% and 49.89%) power coupling to the two output ports.

Width: 13 µm
Length: 152 µm
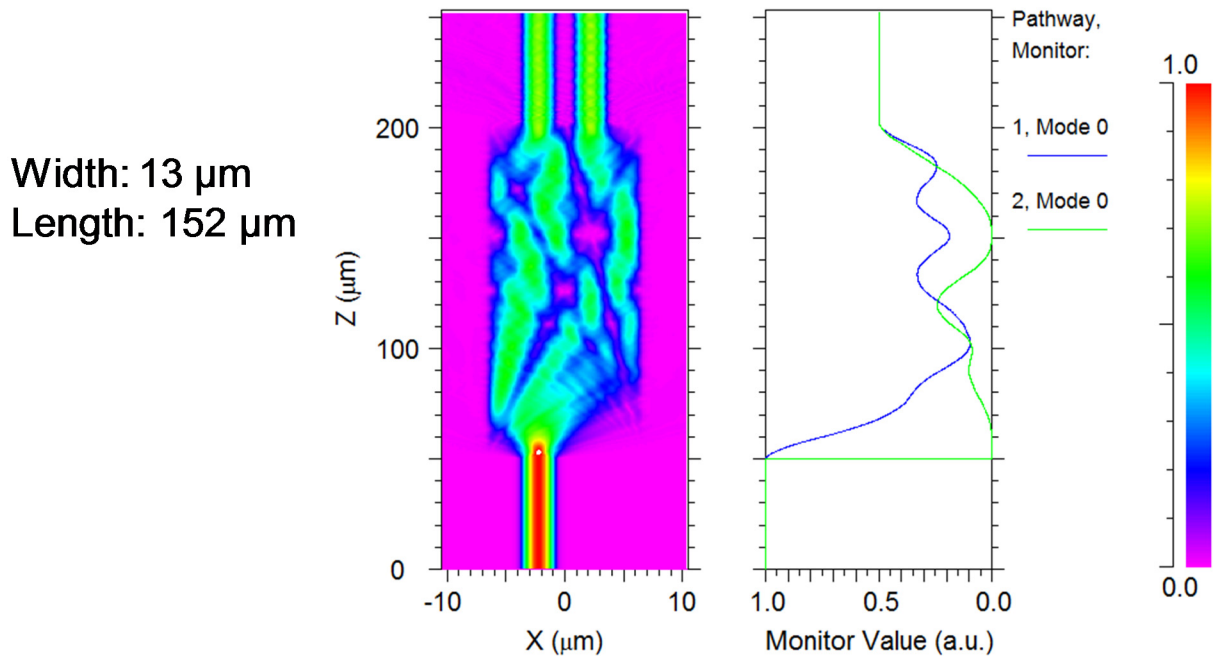
Figure 25. Si₃N₄ 2×2 MMI simulation.

The couplers are very compact, with the 1×2 MMI at 69-µm long and the 2×2 MMI at 152-µm long.

II.D. Image simulations and image reconstruction algorithms

II.D.1. Image simulations

Figure 26 shows the SPIDER modeling and simulation flow chart. The interferometric imaging model and algorithms are based on a model that was developed under Lockheed Martin

IRAD funding for the DARPA Galileo imaging interferometer array. However, since the physics are the same, there are only minor differences in the model components. This model produces raw fringe data with all the appropriate noise sources, including the detectors. The raw fringe data are then fed to the image reconstruction algorithm to produce a simulated image.
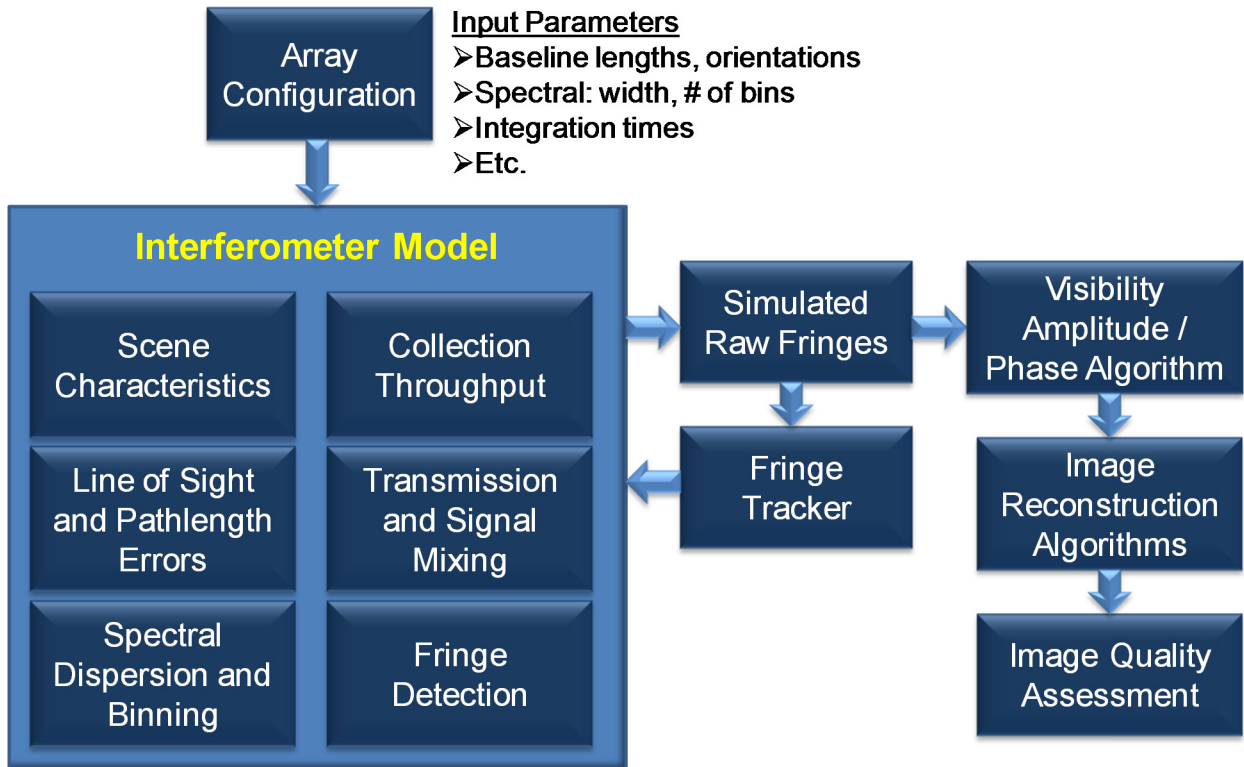
Figure 26. SPIDER modeling and simulation flow chart.

Figure 27 presents the details of the interferometer model. Once a scene model is determined, the model produces raw fringe data with all the appropriate noise sources (including detection noise) which are then fed to the image reconstruction algorithm to produce a simulated image.
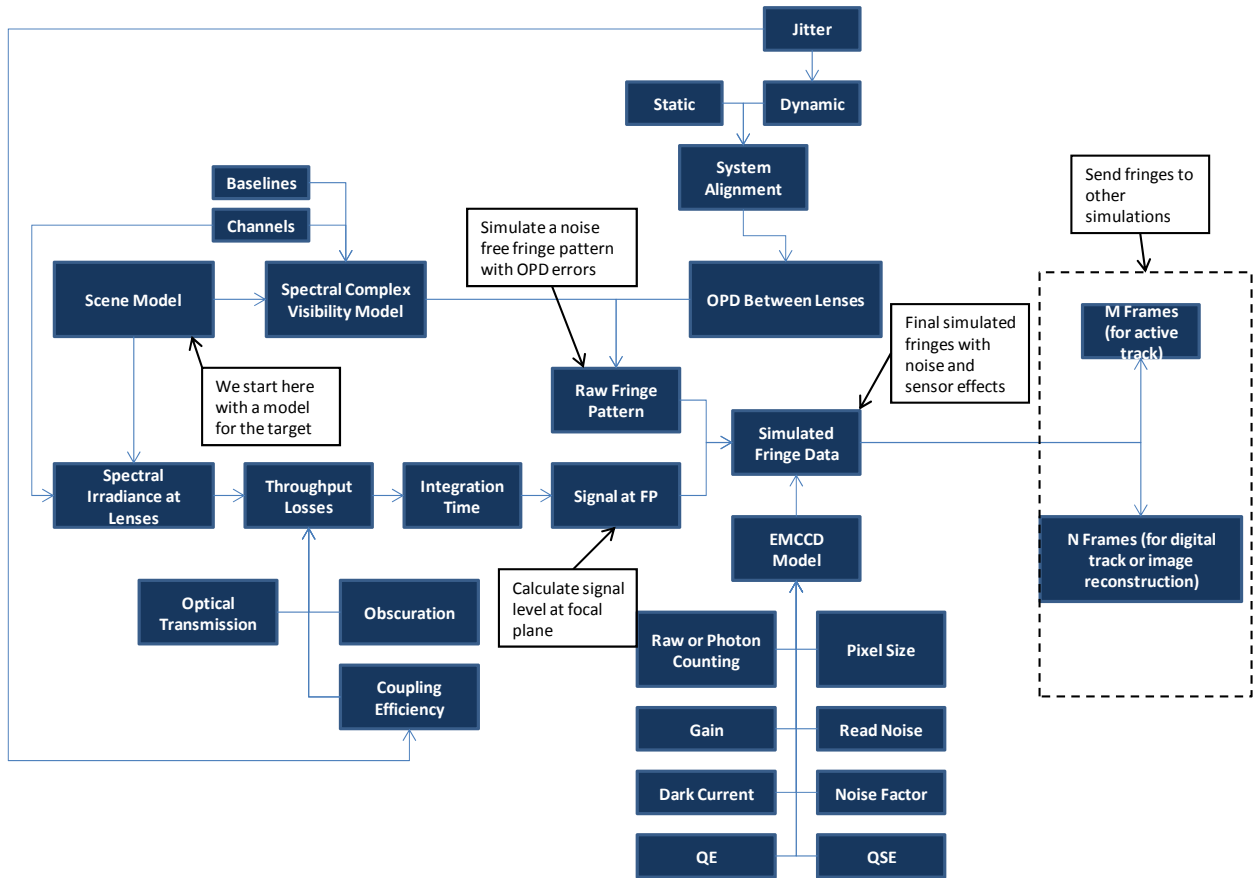
Figure 27. Details of the SPIDER interferometer model from Figure 26.

Figure 28 summarizes the image reconstruction process, the algorithm is a nonlinear optimization algorithm and it begins with an initial object and support estimate computed from the raw fringe data. The algorithm then (a) performs a discrete Fourier transform (DFT) from an object estimate on a Cartesian grid to the locations of the visibility samples in *u-v* space; (b) for each physical baseline, the algorithm optimizes over all of the gain terms, and over constant and linear (in wavenumber) phase terms associated with unknown optical path differences (OPDs) between each pair of apertures, (c) computes a maximum likelihood error metric quantifying the agreement of the model with the given data points, including terms for non-negativity and satisfying the support and other constraints, (d) using an efficient analytic expression for the gradient of the error metric with respect to the unknown object pixel values, it performs a conjugate gradient search to find the object and the gain and OPD-related parameters that best predicts the measured data. In doing that, it fills in missing *u-v* data points in the sparse aperture and corrects for the OPD errors. Finally, the algorithm dynamically re-estimates the support of the object using a "shrink-wrap" algorithm.
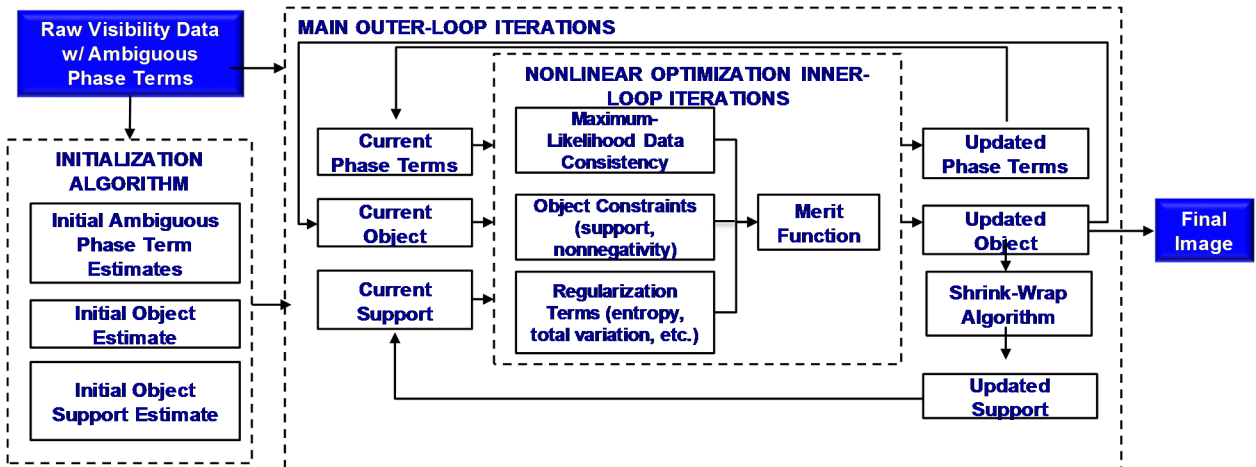
Figure 28. Image reconstruction flow chart. (Developed by University of Rochester (Dr. Jim Fienup) under Lockheed Martin's IRAD funding)

Figure 29 shows example simulated fringe data generated by a model similar to that described above for two different relative optical path difference (OPD) phases (k=0 for 0 rad, k=1 for π rad). Figure 29(a,b) shows the fringe data without noise sources (e.g., electronic and detection noise) and Figure 29(c,d) shows the fringe data with noise sources.
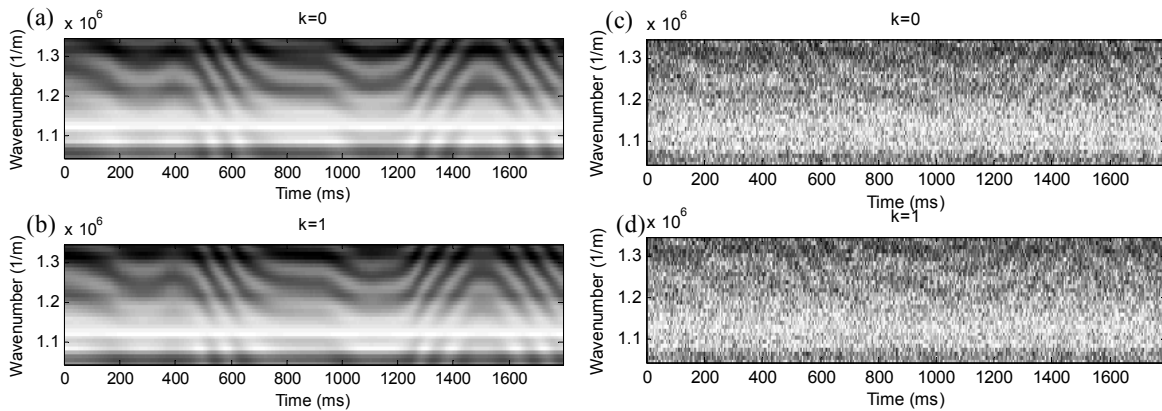
Figure 29. Example simulated fringe data, (a,b) without noise and (c,d) with noise.

II.D.2. *SPIDER image simulations*

Table 1 presents the design parameters used for ground image simulations detailed in the next paragraphs.

Table 1. SPIDER system parameters for ground image simulations.

parameter	value	units	source
lamda (low)	5.00E-07	meters	reference mission
lamda (high)	9.00E-07	meters	reference mission
effective diameter	0.12	meters	reference mission
altitude	3.50E+05	meters	reference mission
x and y ground area coverage	5.00E+03	meters	reference mission
diagonal	7.07E+03	meters	derived
FOV	1.01E-02	radians	derived
FOV	0.58	degrees	derived
GSD	1.02	meters	derived
lenslet diameter	5.00E-03	meters	SPIDER design
lenslet GRD	49.00	meters	SPIDER design
number of waveguides per lenslet(X)	102		derived to meet FOV
number of waveguides per lenslet(Y)	102		derived to meet FOV
number of lenslets	14.00		derived to meet NIIRS
lenslet f/number	18.00		SPIDER design
focal length	9.00E-02	meters	SPIDER design
"pixel" size	2.5E-05	meters	SPIDER design
waveguide array dimension (X)	2.6E-03	meters	SPIDER design
waveguide array dimension (Y)	2.6E-03	meters	SPIDER design
number of uv slices	37.00		SPIDER design
number of spectral bins	10.00		SPIDER design
spectral bin bandwidth	40.00	nm	SPIDER design
total collecting area	1.02E-02	m^2	SPIDER design

Figure 30 shows the analysis of the *u-v* (Fourier) plane coverage for a "basic lenslet pairing" case. Figure 30(a) shows the pairing where the two innermost lenslets form the shortest baseline (i.e., 1 lenslet spacing) and successively pairings of the remaining lenslets form longer baselines (i.e., 3, 5, 7, 9… lenslet spacings). Figure 30(b) shows the calculated *u-v* sample points for each baseline and spectral bin. The sample points overlap well at long baselines, but a small *u-v* gap at low spatial frequencies remains.
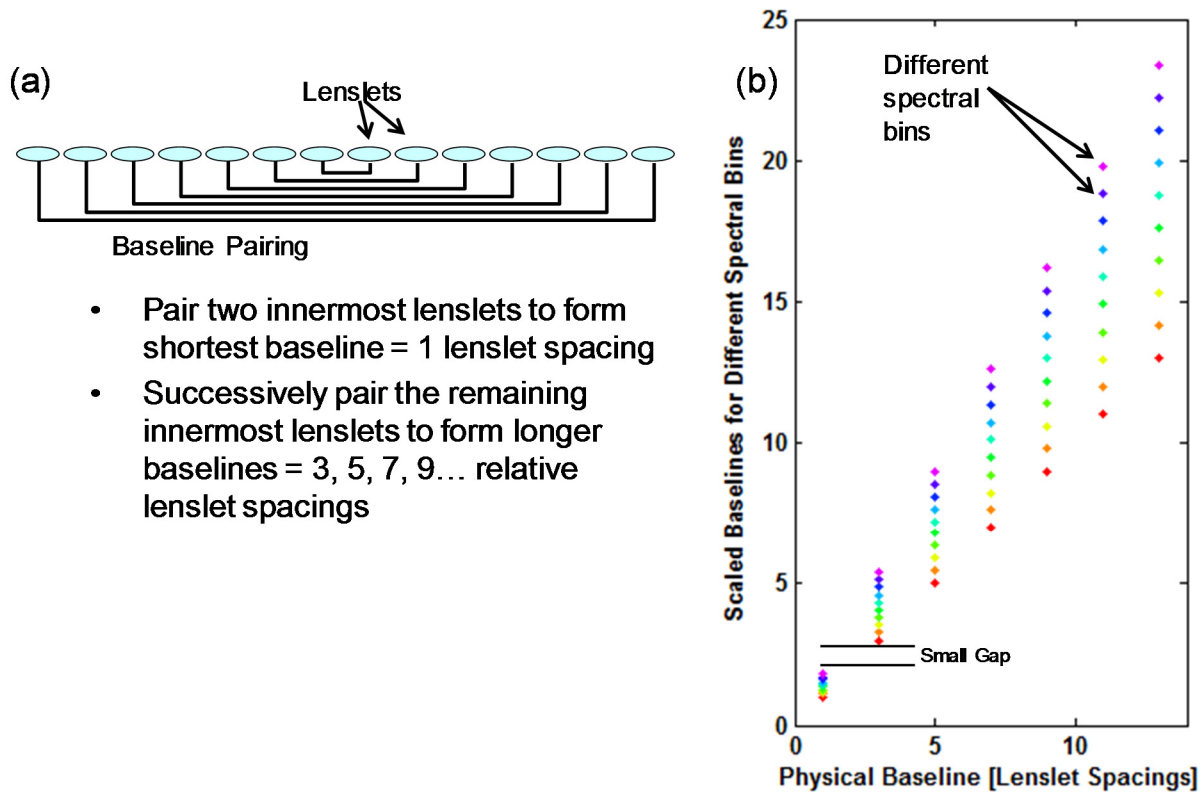
Figure 30. Analysis of *u-v* (Fourier) plane coverage for the "basic lenslet pairing" case. (a) Black lines indicate which lenses are paired together to form a baseline. (b) Calculated *u-v* sample points for each baseline and spectral bin.

To remove this gap it is possible to make a simple pairing adjustment. Figure 31 shows the analysis of the *u-v* (Fourier) plane coverage for a "modified lenslet pairing" case. Figure 31(a) shows the pairing where a lenslet pairing is changed to a baseline of three lenslet spacings. Figure 31(b) shows the corresponding calculated *u-v* sample points for each baseline and spectral bin. The adjusted pairing removes the gap in the *u-v* coverage at the shortest baselines that was present in the previous case. The simulation results that follow use this pairing.

(a)

(b)
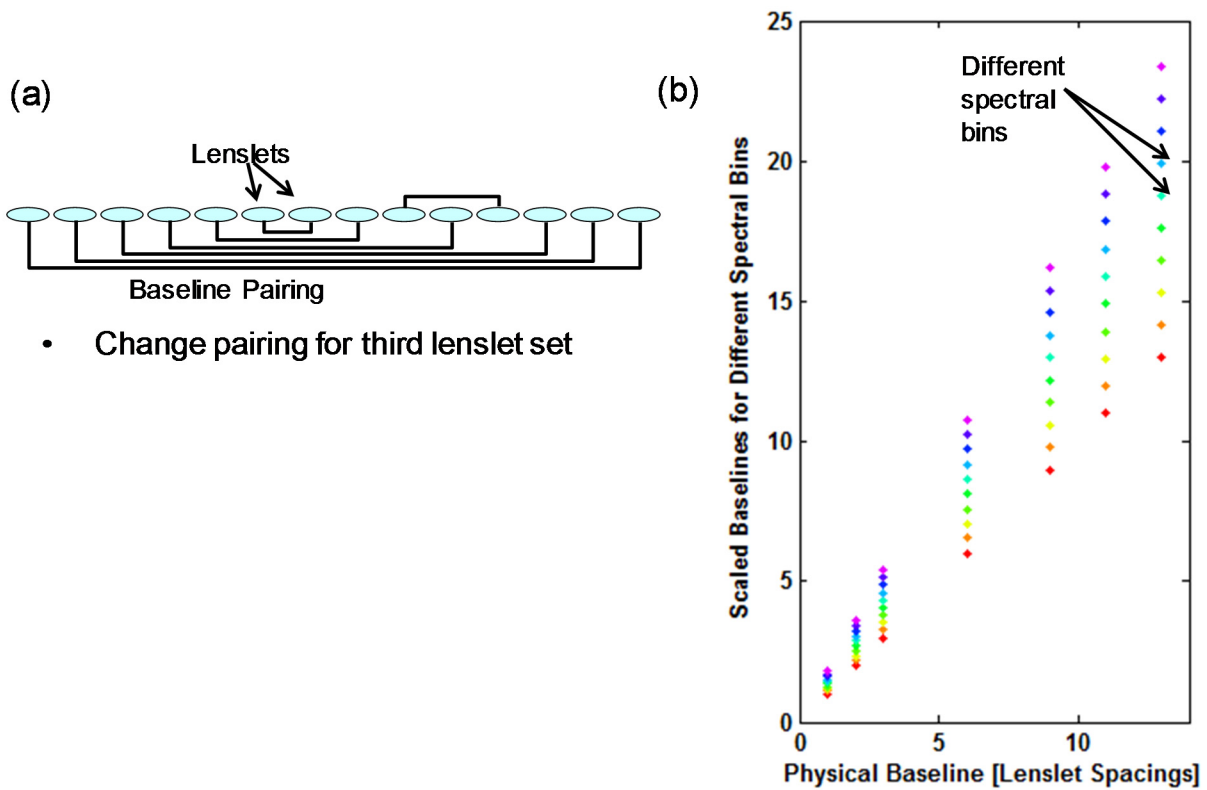
Figure 31. Analysis of *u-v* (Fourier) plane coverage for the "modified lenslet pairing" case. (a) Black lines indicate which lenses are paired together to form a baseline. (b) Calculated *u-v* sample points for each baseline and spectral bin.

Figure 32 shows the scene data used for the imager simulations. It is an image of Judiciary Square, Washington, D.C. and is from USGS High Resolution Orthoimagery (16cm GSD), Collection Date: April 2-3, 2010, (This data is public domain and available from the United States Geological Survey through http://nationalmap.gov).
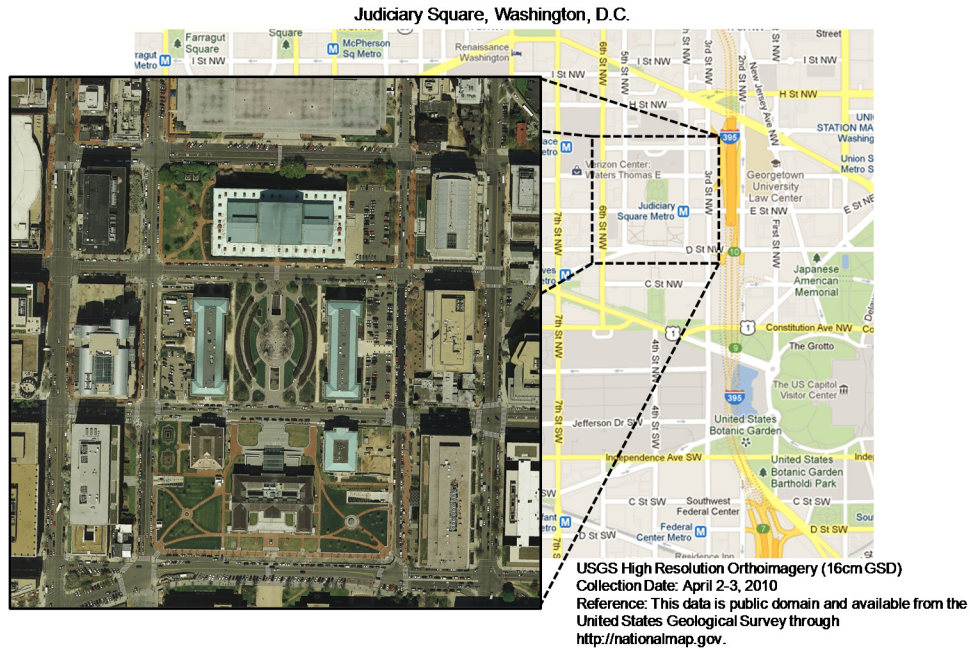
Figure 32. Scene data used for imager simulations.

Figure 33 shows the simulation sequence to create a single sub-image using the imager model. First, the user selects the field of view (FOV) for the sub-image. The sub-image is cropped and the effects of coupling into the optical waveguide are modeled (i.e., image is apodized). Then the *u-v* data are computed and the raw data shown. Finally, the sub-image is reconstructed from the *u-v* data.

1. User selects FOV for sub-image

2. Crop scene and apodize (fiber coupling)

3. Make a conventional comparison sub-image

4. Compute *u-v* data & make "dirty" image

5. Reconstruct sub-image
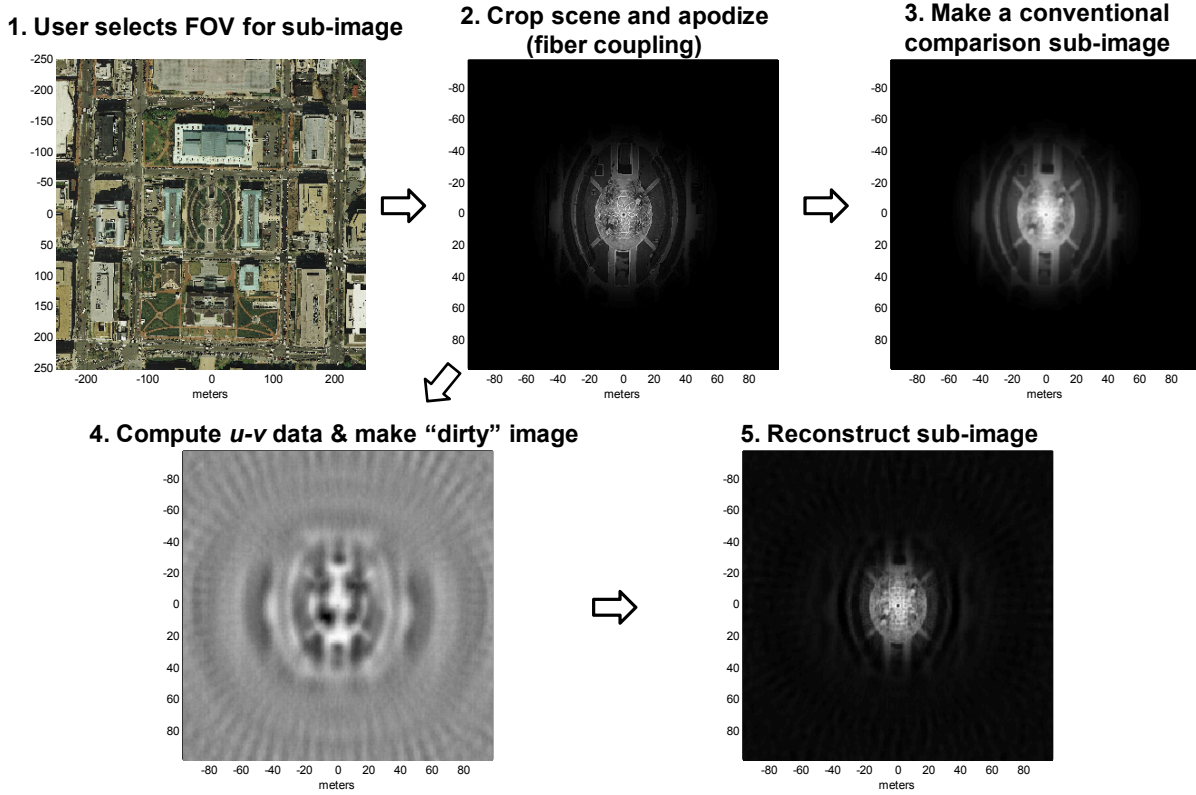
Figure 33. Simulation sequence for a single sub-image.

Figure 34 presents the sub-images from both a conventional imagers and for the SPIDER imager for comparison. As the images demonstrate, the SPIDER sub-image shows finer detail, but the point-spread function (PSF) sidelobes give a slightly noisy appearance (there was no measurement noise in this simulation).

Apodized Scene

Conventional sub-image

SPIDER sub-image

*No Wiener filter applied
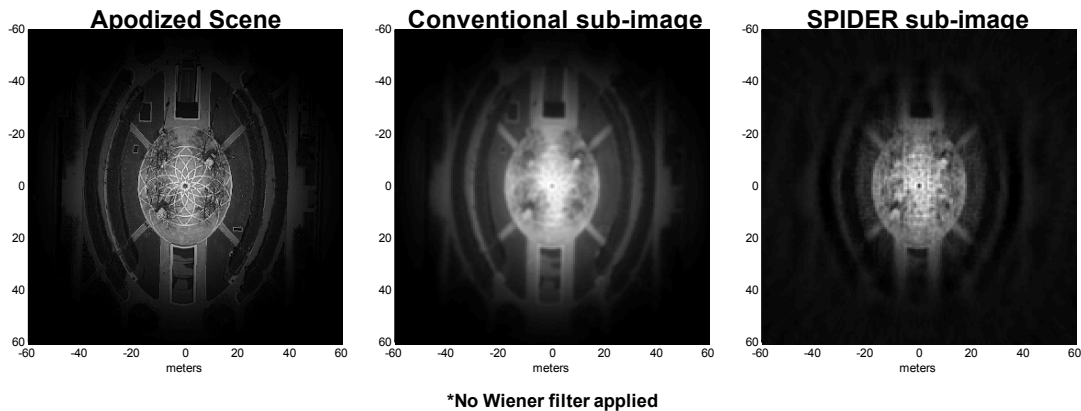
Figure 34. Sub-image comparisons. *****Wiener filter is often used to remove blur in images due to linear motion or unfocussed optics.

Figure 35 shows both the conventional image mosaic and the SPIDER image mosaic for comparison. The "banding" that is visible in the SPIDER image is likely due to the lack of low

spatial frequency *u-v* samples at the lowest frequency (dc) and is fairly straightforward to remove.
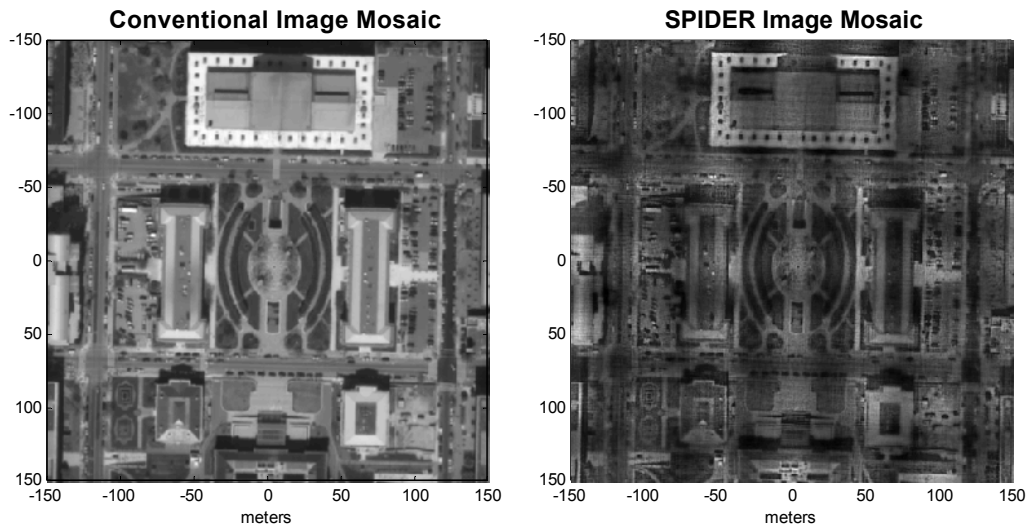
Figure 35. Image mosaic comparison.

Although these image simulations are for a brighter object than Europa (i.e., Earth), they show the essential properties of the SPIDER imager and a typical resulting image.

II.E. Initial fringe data from a silica PIC

Figure 36 shows the heuristic operation of an interferometer where the unresolved sources produce a fringe pattern with a particular fringe visibility and phase (i.e., complex fringe data) that are related to the location of the source(s) (adapted from [9]). Testing of a prototype PIC uses a similar arrangement to verify operation.
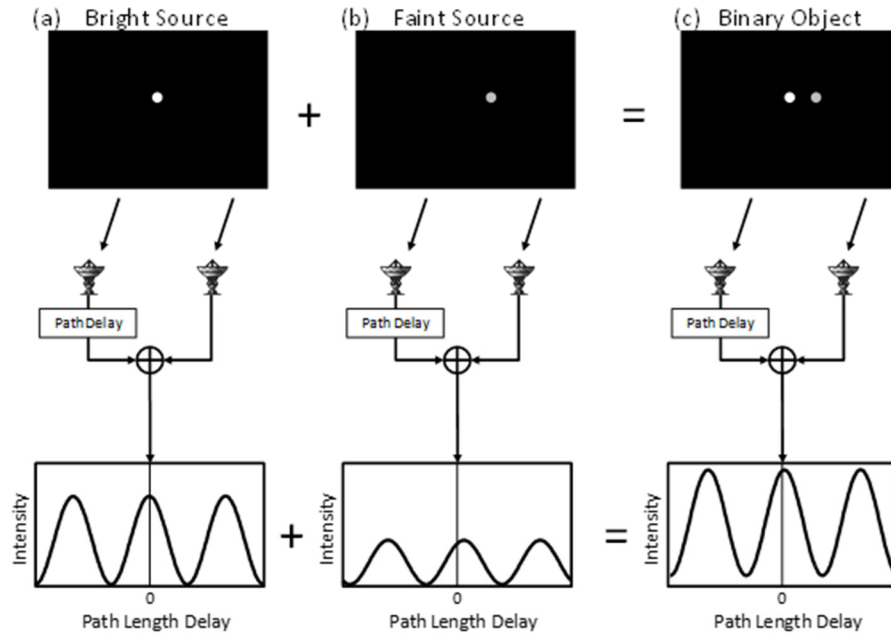
Figure 36. Conceptual operation of an interferometer. (a) Detected fringe pattern from a single bright source. (b) Detected fringe pattern from a single faint source. (c) Detected fringe pattern from a binary source.

Figure 37 presents the experimental arrangement assembled around a prototype PIC (cf., Figure 5) to make fringe measurements. The sources are generated from amplified spontaneous emission (ASE) that is filtered to a bandwidth of 1.2 nm near 1550 nm. Since the pathlengths after the 50:50 splitter are several meters different, the ASE sources are incoherent with respect to one-another (i.e., "white light" sources).
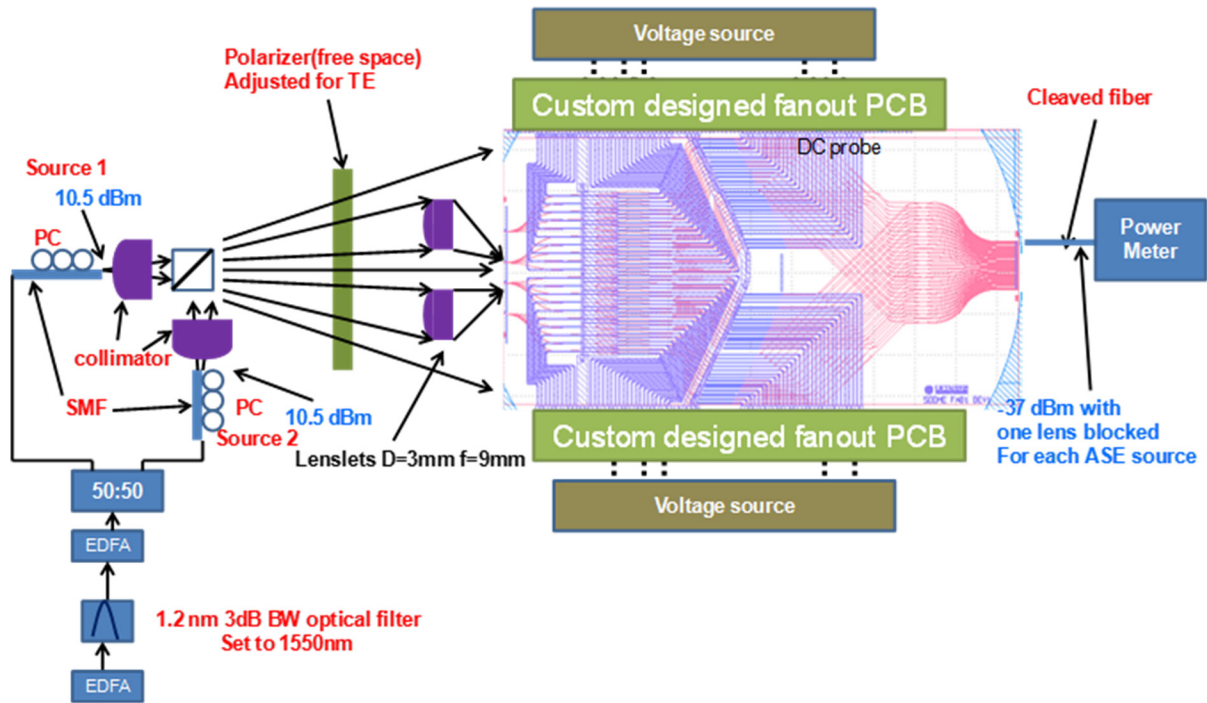
Figure 37. Schematic of the experimental arrangement for fringe measurement with one or two ASE incoherent sources (i.e., white light) and the prototype PIC. SMF: single-mode fiber, PC: polarization controller, EDFA: erbium-doped fiber amplifier.
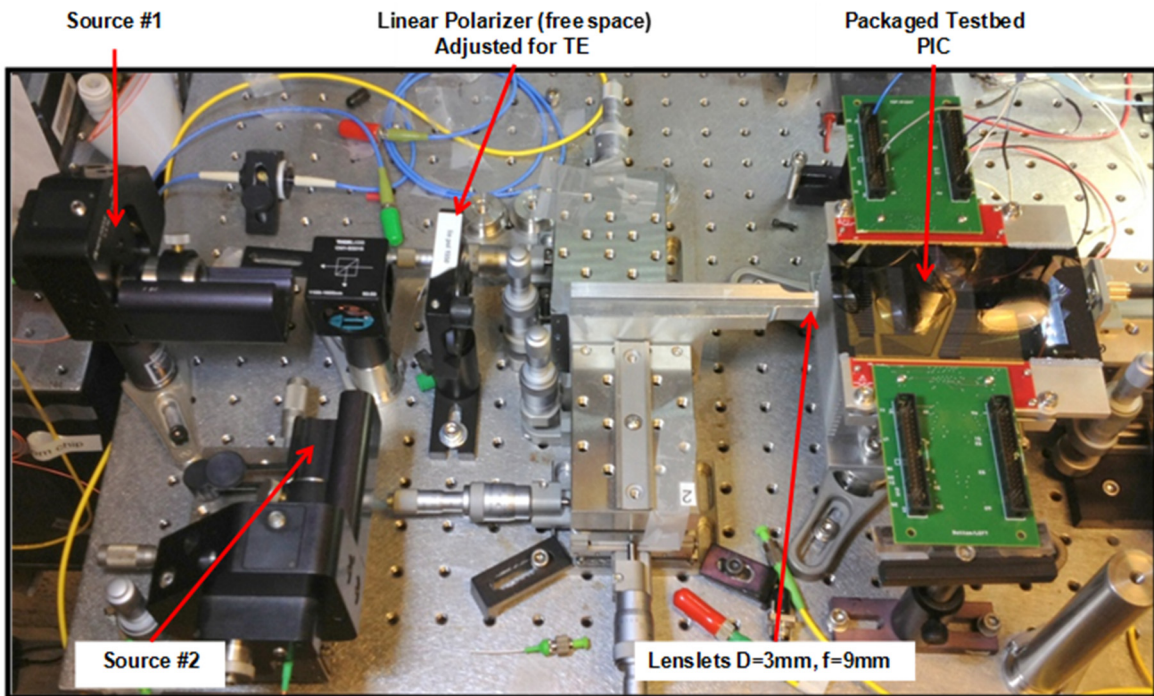
Figure 38. Photo of the experimental arrangement for fringe measurement with one or two independent coherent sources.

Figure 39(a) shows the measured fringe from an incoherent source. Figure 39(b) shows a spectrogram built up from individual measurements of the fringes at different wavelengths.
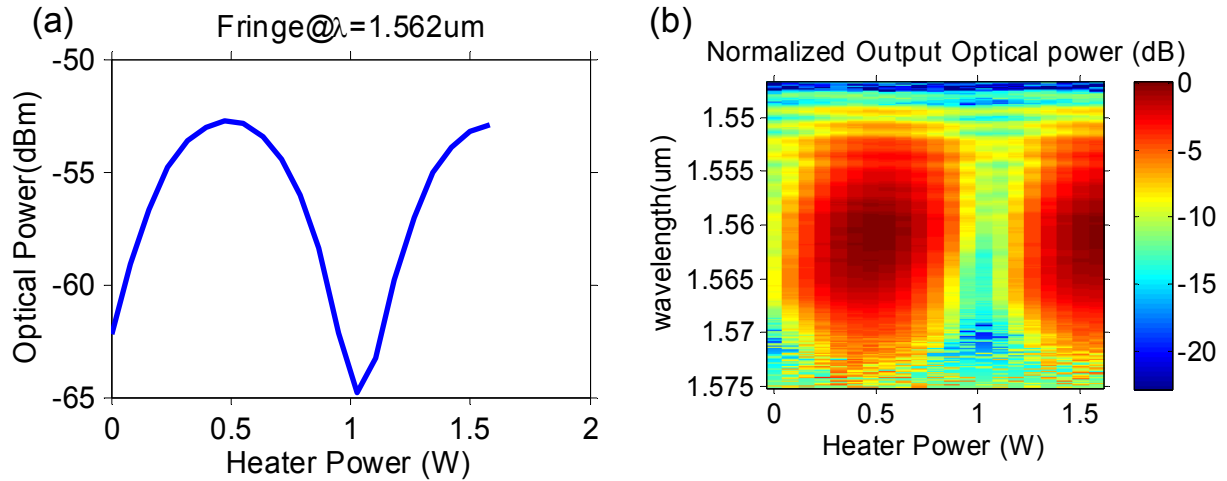
Figure 39. Spectrally resolved fringe measurements. (a) A measured fringe for one incoherent source at λ=1.562 μm. (b) A spectrogram that shows the fringe data for wavelengths from ~1.55−1.575 μm.

Figure 40 shows the measured fringes from one and two incoherent sources (Source 2 in Position 2) where Figure 40(a) shows the intensity data on a log scale and Figure 40 (b) shows the intensity data on a linear scale. The demonstrated extinction of 10−15 dB indicates that the splitters and interferometers are working correctly. The fringes from each source sum correctly (this is a measurement, not a mathematical sum) since the two sources are incoherent with respect to each other.
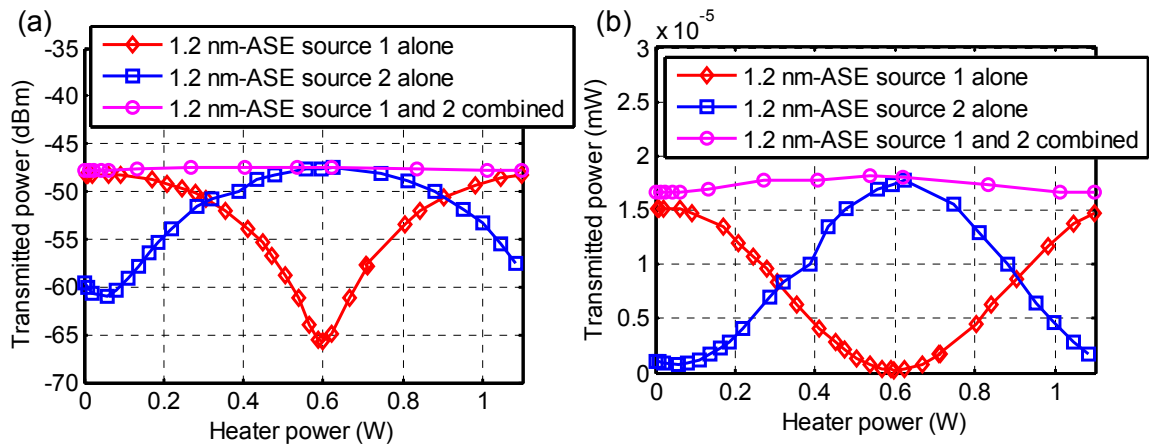
Figure 40. Measured fringes for one and two incoherent sources (Source 2 in Position 2) (a) log scale (b) linear scale.

Figure 41shows the measured fringes from one and two incoherent sources when Source 2 is in Position 2 (notice the fringe phase shift).
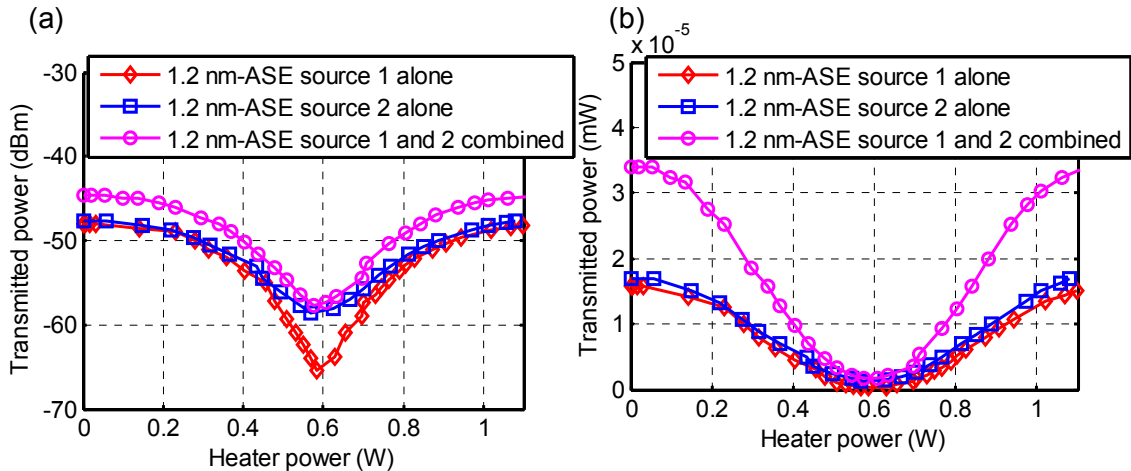
Figure 41. Measured fringes for one and two incoherent sources (Source 2 in Position 3) (a) log scale (b) linear scale.

II.F.   A technology roadmap

Figure 42 identifies some of the technology needs and provides a roadmap to guide further investigation and to show where there is significant leverage of existing technology. By leveraging Lockheed Martin IRAD, commercial industry, DARPA and NASA investments, development costs can be minimized.
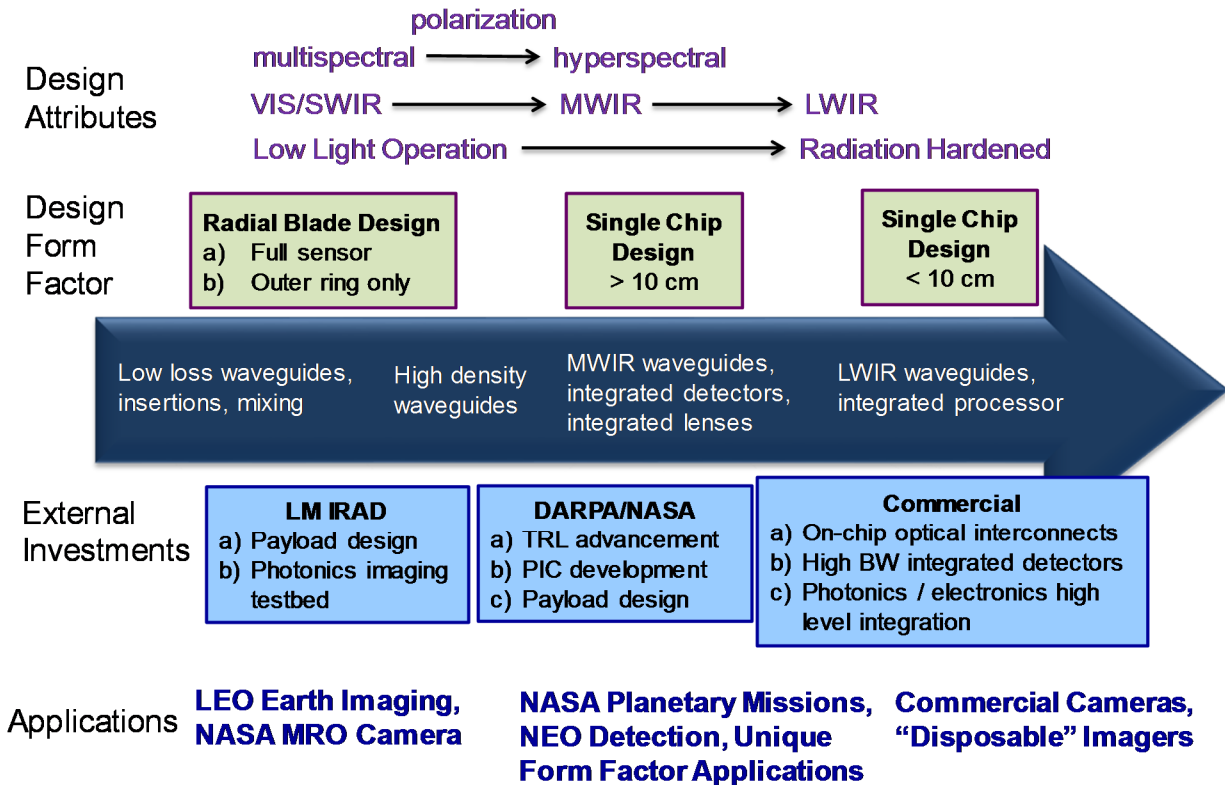
Figure 42. SPIDER technology roadmap.

References

[1] R. L. Kendrick, A. Duncan, C. Ogden, J. Wilm, D. M. Stubbs, S. T. Thurman, T. Su, R. P. Scott, and S. J. B. Yoo, "Flat panel space based space surveillance sensor," in *Advanced Maui Optical and Space Surveillance Technologies (AMOS) Conference*, Maui, Hawaii, 2013.

[2] J. E. Baldwin and C. A. Haniff, "The application of interferometry to optical astronomical imaging," *Philosophical Transactions of the Royal Society of London. Series A: Mathematical, Physical and Engineering Sciences,* vol. 360, pp. 969-986, 2002.

[3] A. Himeno, K. Kato, and T. Miya, "Silica-based planar lightwave circuits," *Selected Topics in Quantum Electronics, IEEE Journal of,* vol. 4, pp. 913-924, 1998.

[4] Enablence. (2012), *Foundry Capabilities*. Available: http://www.enablence.com/components/services/foundry-capabilities

[5] Europa Study Team, "Europa Study 2012 Report," National Aeronautics and Space Administration (NASA) JPL D-71990, 2012.

[6] B. Buffington, S. Campagnola, and A. Petropoulos, "Europa Multiple-Flyby Trajectory Design," in *AIAA/AAS Astrodynamics Specialist Conference*, 2012.

[7] F. P. Payne and J. P. R. Lacey, "A theoretical analysis of scattering loss from planar optical waveguides," *Optical and Quantum Electronics,* vol. 26, pp. 977-986, 1994.

[8] J. Bauters, M. Heck, D. D. John, M.-C. Tien, W. Li, J. S. Barton, D. J. Blumenthal, J. Bowers, A. Leinse, and R. G. Heideman, "Ultra-low-loss Single-mode Silicon Nitride Waveguides with 0.7 dB/m Propagation Loss," in *European Conference and Exposition on Optical Communications (ECOC)*, 2011, p. Th.12.LeSaleve.3.

[9] C. Haniff, "An introduction to the theory of interferometry," *New Astronomy Reviews,* vol. 51, pp. 565-575, 2007.